Valorization of surface-water RO brines via Assisted-Reverse Electrodialysis for minerals recovery: performance analysis and scale-up perspectives

A. Filingeri[a,b], M. Philibert[c*], E. Filloux[c], N. Moe[d], A. Poli[c], A. Tamburini[a,b], A. Cipollina[a,b*]

[a] Dipartimento di Ingegneria, Università degli Studi di Palermo, Viale delle Scienze Ed. 6, 90128 Palermo, Italy.

[b] ResourSEAs SrL, Viale delle Scienze, Ed.16, 90128 Palermo, Italy.

[c] SUEZ - CIRSEE, 38, rue du Président-Wilson, 78230 Le Pecq, France.

[d] SUEZ-WTS, 5951 Clearwater Dr, Minnetonka, MN 55343, USA.

[*]Corresponding Authors. E-mail: andrea.cipollina@unipa.it, marc.philibert@suez.com

ABSTRACT

Reverse Osmosis (RO) processes have been recently identified as mostly capable of quantitative removal of salts and contaminants from saline and surface waters, though posing the problem of a concentrated brine to be disposed of and a produced permeate too low in minerals, thus requiring a sometimes expensive remineralization step. In the present paper, Assisted-Reverse Electrodialysis (A-RED) has been proposed for the remineralization of surface-water RO permeate by recovering minerals from its brine. A purposely developed and validated model has been adopted to carry out a parametric analysis for design and optimization of an industrial-scale plant. The techno-economic analysis underlined that full permeate remineralization can be achieved with minimum specific consumption of 0.08 kWh m^{-3}, while a minimum remineralization cost of 2.1 c€ m^{-3} was found applying a permeate by-pass and feed & bleed scheme to (i) increase the plant remineralization capacity and (ii) maintain a stack inlet conductivity above 100-160 µS cm^{-1} (starting from a permeate ~10 µS cm^{-1}). Compared to current post-treatment techniques, results appear very promising thanks to the reduction of total costs, chemicals and environmental concerns related to brine disposal.

1. INTRODUCTION

Reverse osmosis (RO) plays a key role in the field of seawater and brackish water desalination [1,2], while recently gaining more and more attention in the field of surface water potabilization [3,4]. However, two important issues affecting process sustainability are the disposal of the concentrated brine it produces and the need for chemicals for permeate remineralization. Concentrated brines are often disposed of in the environment, although Zero Liquid Discharge approaches are gaining more attention [5–7]. Indeed, RO untreated permeate cannot be directly used as drinking water due to its very low TDS value, which makes the permeate aggressive and unpalatable (WHO standards [8]). Therefore, desalted water requires one or more remineralization steps for pH and alkalinity correction and addition of minerals such as calcium and magnesium, important for human health and to prevent corrosion in the pipelines [9,10]. Post-treatment may involve disinfection [11] and/or degasification depending on the desalinated water quality. The Israeli Ministry of Health defined the following four parameters as water quality targets (all as equivalent $CaCO_3$ concentration): Alkalinity > 80 mg l^{-1}, 80 mg l^{-1} < $[Ca^{2+}]$ < 120 mg l^{-1}, $CaCO_3$ Precipitation Potential (CCPP)[1] in the range of 3-10 mg l^{-1} and pH< 8.5 [12]. In conventional remineralization, one of the approaches that is gaining more and more attention is the use of calcium carbonate particle beds, whose dissolution kinetics are enhanced by the reduction of pH, often carried out through the addition of CO_2 [13,14]. Subsequently, the pH is adjusted to reach the final target, often by the addition of NaOH [15], although less common practices are CO_2 stripping [16] and the use of $Ca(OH)_2$ [17]. In the Daoura plant, a hardness of 5°f (in conformity with Moroccan standards) was obtained using only a calcite bed, without any prior acidification and, thus, in the absence of final NaOH injection [18]. Direct dosing of chemicals can be carried out by the addition of $Ca(OH)_2$ and CO_2 to increase both water alkalinity and hardness, which is the most common post-treatment in desalination plants, although lime is more expensive than calcite and the process consumes more CO_2 [19]. Other chemicals such as $Ca(OH)_2$+$NaHCO_3$ or $CaCl_2$+$NaHCO_3$ can be adopted, though they are more expensive [17] and add large quantities of undesirable ions such as sodium and chlorides [20], whose presence can be a problem especially if

---

[1] CCPP is a quantitative indication of the solution potential to precipitate or dissolve $CaCO_3$(s) [55].

the water is used for irrigation. Another suggested method is the blending of the RO permeate with a small percentage of seawater, brackish water or groundwater to raise its mineral content [21]. The cost of post-treatment steps is a function of the selected process, desired water quality target and plant capacity, but they often represent up to 10% of the total cost of the produced water [17]. As an example, the cost of remineralization using hydrate lime and carbon dioxide for an hypothetical SWRO plant with a capacity of 100,000 m^3 day^{-1} [22] and a SWRO desalination plant located in Morocco [23], summed up to 5.8 c€ m^{-3} and 6.5 \$cents m^{-3}, respectively, while a cost of 4.9-5.4 \$cents m^{-3} was estimated at pilot scale, where acidification was performed with H_2SO_4 [24]. In 2021, Kim et al. [25] proposed the use of acetic acid, as a substitute for H_2SO_4 or CO_2, coupled with calcite dissolution and UV treatment for small-capacity desalination plants with an estimated cost of 6.4 \$cents m^{-3}. However, all the options listed above are based on the use of external chemicals, disregarding the fact that all salts necessary for the remineralization are in principle already present in the brine discharged from the same plant [26]. Rijnaarts [27] patented the extraction of a divalent cation-rich solution from the feed stream by the coupled use of Donnan dialysis and nanofiltration, which can be deployed for remineralisation of RO permeate. Recently, much more attention has been paid to the addition of magnesium, which is nowadays only added in a few plants around the world, thanks to the fact that the Israeli Ministry of Health has required a minimum magnesium concentration of 20 mg l^{-1} in drinking water, considering its importance for human health [17]. Tang et al. [28] proposed the combination of two steps of nanofiltration and diananofiltration for the addition of 20 mg l^{-1} of Mg^{2+} and 2.7 mg l^{-1} of Ca^{2+} at a cost of 1.7 \$cents m^{-3}. As an alternative, the authors proposed Cation Exchange Resin coupled with diananofiltration to enrich desalinated permeate in magnesium [29] at a concentration of 20 mg l^{-1} and a cost of 3.2 \$cents m^{-3}, which is higher compared to the previous work but justified by a lower concentration of sodium and chloride in the remineralized permeate. In 2020, the same authors proposed a hybrid nanofiltration-diananofiltration-electrodialysis process scheme to separate a Mg-rich solution from seawater [30], to be used for magnesium enrichment of desalinated water, with a cost of 1.4 \$cents m^{-3}.

In recent years, electro-membrane processes have been proposed for use in desalination, pre-desalination and post-treatment of brines. Electrodialysis (ED) application is mainly restricted to brackish water desalination, though significant advances in the manufacture of new high-performance membranes and in process optimization are promoting ED as an alternative technology for seawater desalination as well [31–33]. A more recently proposed electro-membrane process is Reverse Electrodialysis (RED), which has been studied for the production of electric energy from the "controlled mixing" of two solutions at different concentrations [34,35]. Derived from RED, the

Assisted-Reverse Electrodialysis (A-RED) process is based on the application of an external voltage to enhance salt passage in the direction of the spontaneous flux of ions from the concentrate to the dilute solution, in order to increase the process performance and reduce the required membrane area, though an increase in the specific energy consumption of the process is generated [36]. ED, RED and A-RED were proposed as a pre-desalination step for RO in order to reduce energy consumption [37,38] or as a post-treatment step for brine valorisation [39,40] or for increasing water recovery of desalination plants [41], and for the removal of boron form of elements as boron [42].

A new application of the A-RED process is proposed for the remineralization of the RO permeate, recovering minerals from the RO brine. The A-RED process (see Figure 1) is suitable for this process, as it implies the application of an external voltage in the same direction as the concentration gradient (between adjacent channels), thus enhancing the passage of "useful" ions (i.e. minerals) from the brine to the permeate through the ion exchange membranes. Conversely, larger organic molecules are rejected thereby avoiding contamination of the permeate. The proof-of concept of this new A-RED application was demonstrated at the laboratory scale using synthetic and real solutions supplied, as output, from a Low Pressure Reverse Osmosis unit: in particular, this unit produced a brine rich in bicarbonates from the desalination of Seine River surface-water [43]. The results confirmed the technical feasibility of adopting A-RED as a remineralization technology complying with required legislative standards and maintaining high rejection against organics and micropollutants. Worth noting that the conditions of implementation of this technology will strongly depend also on the specific features and composition of the RO brine produced, and may benefit, for example, from the use of ionic exchange membranes with enhanced selectivity to divalent ions.

However, the economic feasibility of this novel approach is still missing in the literature. The present work is devoted to fill this gap by performing for the first time a techno-economic assessment of the proposed process. More precisely, an A-RED model has been re-adapted, validated with laboratory-scale experimental results, and eventually used to perform broad parametric analysis devoted to guiding the design and operation of an industrial-scale A-RED plant.
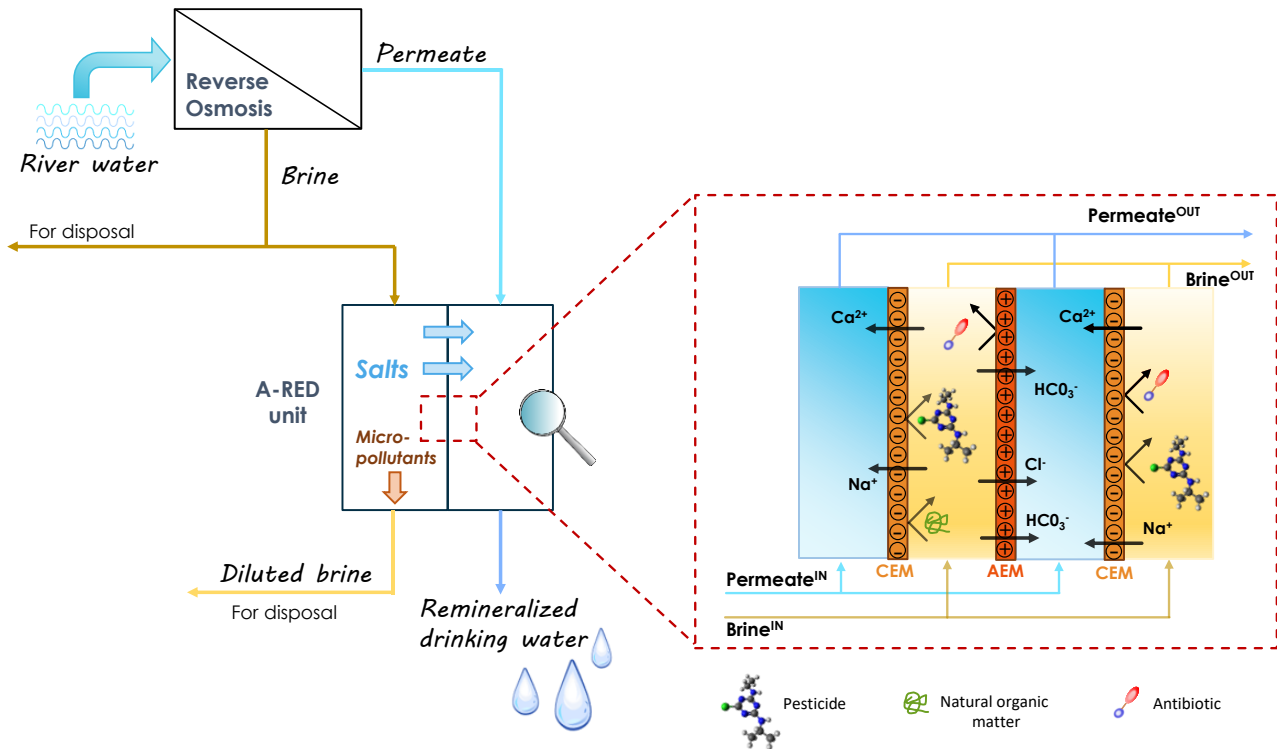
Figure 1 Schematic of the proposed process for remineralization of RO permeate through recovery of minerals from RO brine via Assisted-Reverse Electrodialysis (adapted from [43]**).**

2. Modelling and simulation strategy

2.1 A-RED model description and validation

2.1.1 Model description

An Assisted-Reverse Electrodialysis model previously developed by the same group [44,45] has been readapted for the simulation of the remineralization process. The simulation tool consists of a multi-scale model: a lower scale set of equations on mass and momentum transfer phenomena deriving from Computational Fluid Dynamics (CFD) simulations are used as input for the higher scale A-RED process simulator whose equations are discretized along the streamwise direction (i.e. one dimensional model). More precisely, at the channel level, local information in the form of correlations for the friction factor and the Sherwood number are used for the calculation of pumping losses and concentration polarization factor at the higher scale. The higher scale model calculates global parameters characterizing the operations of the A-RED unit as a whole, starting from fluxes and mass balance calculations at the cell pair level. Notably, the two feed streams are assumed in co-current

arrangement in the model. For the sake of brevity, the model details are reported in Appendix A, while the complete set of equations and information can be found in the literature [44,45].

This multi-scale approach offers a great advantage in terms of robustness and computational speed: it provides good accuracy thanks to the incorporation of local information, estimated even for complex channel configurations including the presence of spacers [45] or profiled membranes [46]. The model can simulate A-RED unit operations at any scale, from laboratory, up to pilot or industrial scale, and can be arranged to simulate single and multistage units.

2.1.2 Model calibration and validation with laboratory experiments

Following its adaptation, the A-RED model was validated with experimental data collected at laboratory-scale. A 5 cell-pair SUEZ-WTS stack was equipped with CR67T and AR204T SUEZ-WTS membranes as cation and anion exchange membranes, respectively, with an active area of 0.028 m^2 separated by spacers 762 µm thick. SUEZ-WTS CR67T-AR204T membrane properties are reported in Table 1

Table 1. Tests were performed in A-RED continuous mode for the remineralization of a RO permeate by recovering minerals from the corresponding brine. Increasing steps of voltage were applied in the same direction as the spontaneous ion transport from the brine to the permeate solution to increase ion passage. A multimeter was connected in series with the stack to measure the corresponding current. The experimental tests used for model calibration and validation were performed with synthetic single-salt ($NaHCO_3$) and mixed salts solutions, mimicking the brine conductivity and composition obtained by treating Seine River water with three RO stages. The velocity of the two solutions in the channels was fixed at $\approx$2 cm s^{-1}. Inlet conductivities for tests with single-salt solutions were 77 µS cm^{-1} and 3.0 mS cm^{-1} for permeate and brine, respectively, while for mixed-salt solutions they were 42 µS cm^{-1} for the permeate and 2.2 mS cm^{-1} for the brine. A more detailed description of the experimental set-up and procedure, and the solution composition are reported in Appendix B, while a complete set of information can be found in a previously reported study [43].

SUEZ-WTS CR67T-AR204T membrane properties (see Table 1) were adopted in the model for the validation and simulation campaign. As a simplifying assumption, the streams generated by the RO unit treating the Seine River water are considered as composed of $NaHCO_3$ only, being this latter the main component (see Appendix B).

Table 1. Reference properties of SUEZ-WTS ion-exchange membranes considered in the present study.

	Thickness (dry) [μm]	Areal resistance[a] [Ω cm^2]	Permselectivity[b] [%]	IEC[c] [meq/g]	Stability pH
AEM: AR204T	280	1.7	89	2.43	1-10.5
CEM: CR67T	300	2.5	86	2.55	1-14

[a] Measured in 0.1N NaCl solution.
[b] Obtained at 0.5/1.0 M NaCl.
[c] expressed as meq/dry g resin.

The model was calibrated with experimental results obtained with single NaHCO$_3$ salt tests and then validated with synthetic mixed-salt solution mimicking the Seine River brine composition. Membrane resistance, r_{IEM}(Ω m^2), was expressed as a function of the more dilute solution concentration, as proposed by Galama et al. [47], as:

$$r_{IEM} = r_{IEM}^{ref} + \frac{a}{C^n}$$

(1)

where r_{IEM}^{ref}(Ω m^2) is the reference membrane resistance (Table 1), C is the (mol m^{-3}) concentration of the dilute stream (chosen step by step as the most diluted between the permeate and the brine during the unit operation). The constant a (= 0.0097) and n (= 1.182) were obtained by calibrating the model with the experimental data collected feeding the A-RED unit with artificial streams composed of NaHCO$_3$ only. The above empirical correlation can be assumed valid for concentrations in the range of 0.1 - 40 mol m^{-3}.

Figure 2 reports the comparison between the model predictions and experimental results collected with artificial solutions (i) either composed of NaHCO$_3$ only (Figure 2a,b) or (ii) mimicking the composition of real streams (Figure 2c,d). Figure 2a and Figure 2c report the current density as a function of the applied voltage for the two cases. The current density increased with the voltage with a gradually decreasing slope, denoting a diminishing stack resistance, as expected due to the outlet permeate conductivity increase, which reduces the average resistance of the dilute compartment. Error bars of the experimental data were obtained by determining the standard deviation of multiple reproducibility tests performed under similar conditions. Very good agreement between the model predictions and experimental measurements was observed with an average deviation between model and experiments of $\approx$3% and $\approx$20% for single-salt and mixed-salts solutions, respectively, which was comparable with the average standard deviation of $\approx$10% in the experimental results. Figure 2b and 2d show the trend of both brine and permeate outlet conductivities as a function of the current density. As expected, an increase in the current density corresponds to a higher ion flux from the brine to the permeate, thus leading to a higher reduction of the brine outlet conductivity and to an increase in the permeate outlet one. More importantly, for both tests (Figure 2b and 2d) the average deviations

between model predictions and experimental results for permeate and brine outlet conductivities were in the range of $\approx$1%-10%, thus highlighting the high predictive capability of the adopted model.
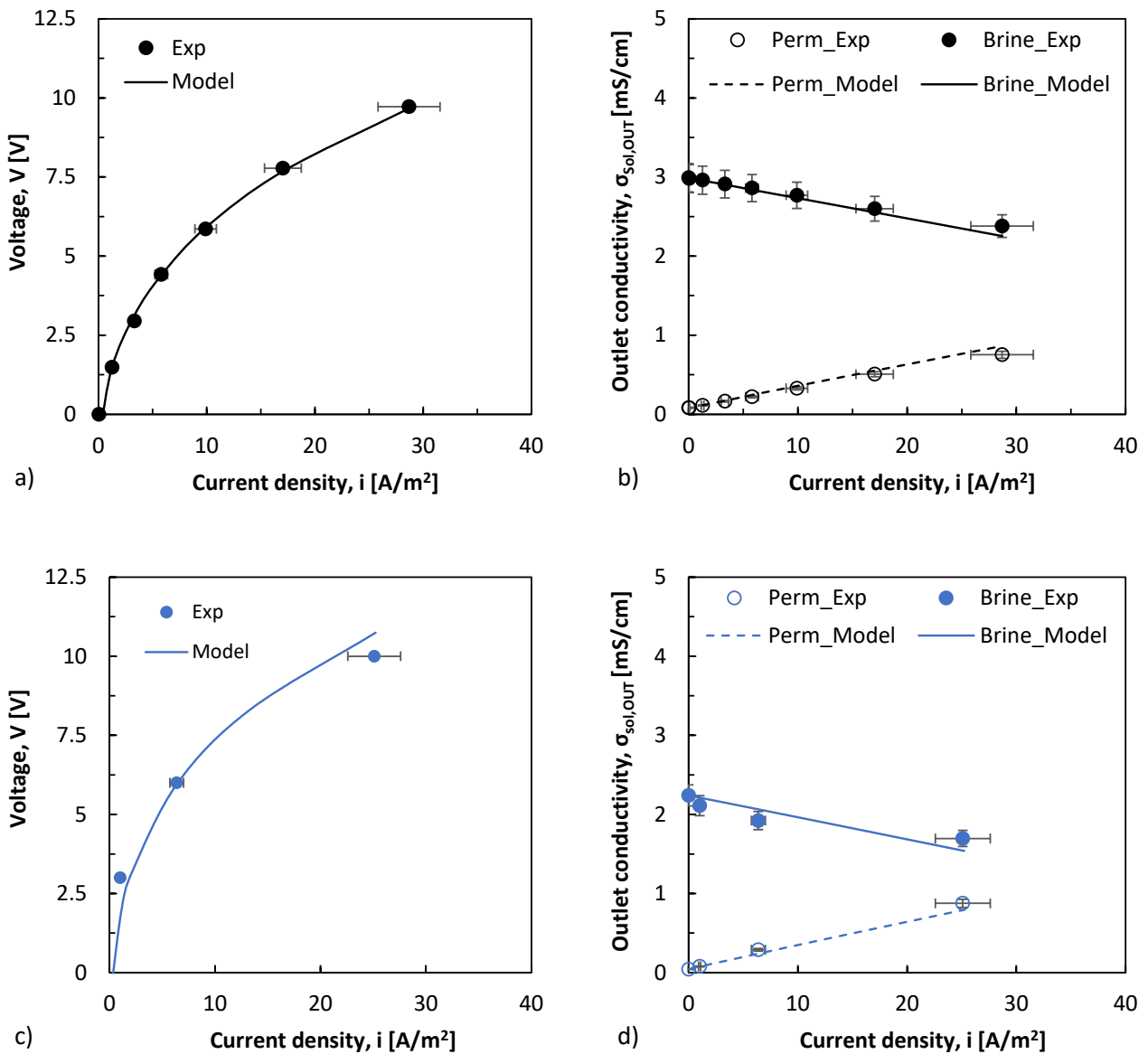
Figure 2. Comparison between experimental data (symbols) and model predictions (curves). Tests performed with solutions composed of NaHCO₃ only (a and b) or mixed-salts solutions mimicking the composition of real feeds (c and d).

2.2 Simulation settings and strategy

The simulation tool was used to perform a sensitivity analysis for a large-scale A-RED unit. The existing RO pilot plant desalinating the Seine River water had a recovery of 85% and produced permeate and brine streams with conductivities of $\cong 10$ µS cm^{-1} and $\cong 3.0$ mS cm^{-1}, respectively. Two outlet permeate conductivity targets of 260 µS cm^{-1} (namely *target A*) and 186 µS cm^{-1} (namely

8

target B) were set to explore the A-RED remineralization capability: these values should be regarded as equivalent to hardness values of 13°f and 9°f (130 mg l^{-1} and 90 mg l^{-1} of hardness as $CaCO_3$, observed via a laboratory calibration with real saline solutions), respectively, matching typical target remineralization values for several European countries, France included [26,48].

2.2.1 Stack characteristics and proposed layouts

Two commercial industrial SUEZ-WTS stacks in series were considered in the simulated plant, equipped with SUEZ-WTS CR67T-AR204T membranes, already tested at the laboratory scale for the model validation (properties are reported in Table 1). The industrial stack geometrical features are reported in Table 2. Note that the number of cell pairs adopted is typical of pilot plant units as an immediate exploitation of the model predictions will be used for pilot plant construction and testing of the process. However, these results are purposely reported in normalized form in the present paper and can be directly extended to industrial-scale stacks with a much high number of cell pairs.

Table 2. Main features of the A-RED stack simulated in the present work.

| Channel length, L [cm]	Channel width, b [cm]	Number of cell pairs per stack, n_{cp}	Spacer thickness, δ [µm]	Spacer porosity, ε [%]
178	18.8	70	762	87

Applied voltages ranging from 14 V (0.2 V/CP) up to 168 V (2.4 VCP) were adopted. Voltage values higher than 1 ΔV/CP were not recommended by the unit manufacturer and were explored for future perspective purposes. Moreover, different units and manufacturers may be able to operate beyond this suggested value.

All of the simulations were carried out with a value of fluid velocity equal to10 cm s^{-1} in both channels (i.e. the brine channel and the permeate one) as recommended by the unit manufacturer. This fixed velocity corresponds to a fixed flowrate entering the stack of 3.6 m^3 h^{-1} for both permeate and brine compartments. In plate & frame membrane modules, comparable channel geometry and flow rates in the two channels are typically adopted to avoid any pressure gradients between the two membranes sides, thus reducing possible internal leakage issues. In order to evaluate the effect of different operating conditions on the specific energy consumption and total process costs, the permeate flow rate was let to vary between 3.6 m^3 h^{-1} and 42.5 m^3 h^{-1}, while the corresponding brine flow rate was 5.7 times lower due to the RO recovery fixed at 85% (brine flow rates in the range of 0.6-7.5 m^3 h^{-1}).

Clearly, the above values were chosen in order to match the typical operative range of the upstream RO unit. Moreover, in the simulated A-RED unit, a feed & bleed operational mode was adopted for the brine when necessary to achieve higher flow rates, while bypass loops for the permeate were added to deal with the exceeding permeate flowrates. On the basis of these conditions, four different layouts recently patented [49] (see Figure 3) were proposed and analysed.

The four adopted schemes, graphically shown in Figure 3, are detailed below.

- Figure 3a shows a configuration with a feed & bleed loop for the brine stream, which allows maintaining the same flow rate in the permeate and brine compartments of the stack;
- Figure 3b shows a scheme including an additional feed & bleed loop on the permeate stream, aiming at increasing the inlet conductivity (thus reducing the electrical resistance) of the permeate channels;
- Figure 3c shows a permeate bypass loop added to the Figure 3b configuration, which allows to increase the total permeate flow rate remineralized after the mixing of the by-pass with the permeate stream exiting the A-RED unit;
- Figure 3d shows a particular sub-scenario of case 3c: when the total brine flow rate arriving from the RO plant exceeds $3.6 \ m^3 \, h^{-1}$, the brine recirculation loop is not needed anymore, thus leading some of the RO brine to be discarded without passing though the A-RED plant.
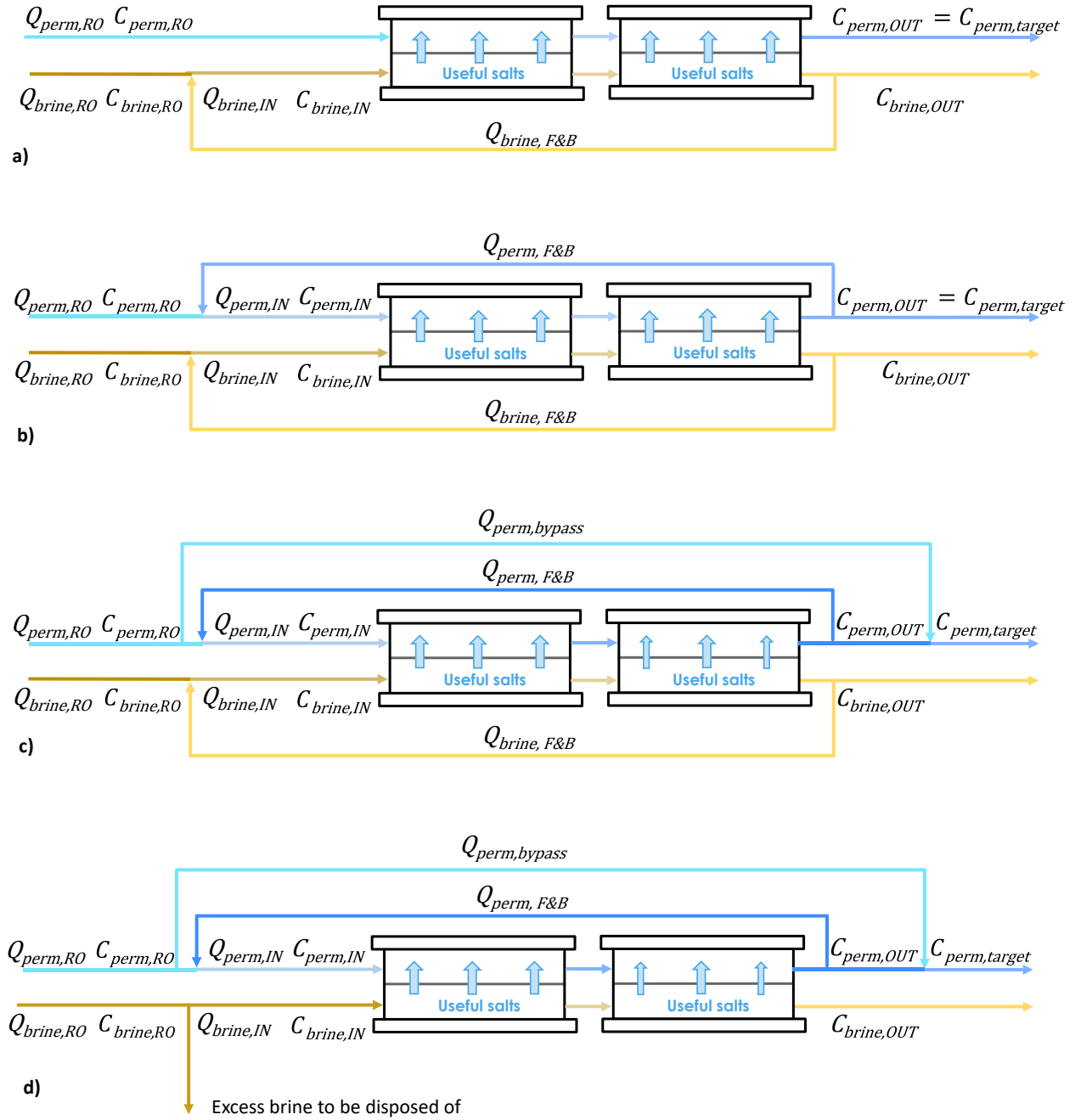
Figure 3. Simulated system configurations with: a) brine feed & bleed loop; b) feed & bleed loops for both brine and permeate; c) feed & bleed loops for both brine and permeate and bypass for the permeate; d) permeate feed & bleed loop and bypass for the permeate.

Of course, the A-RED model was suitably modified in order to simulate the above 4 layouts: for all the above-mentioned schemes, mass balance equations at the nodes generated by recirculation or by-pass loops have been used in order to calculate flow rate and concentration of all relevant streams. In particular, when a brine feed & bleed loop is implemented in the scheme (Figure 3a, Figure 3b, and Figure 3c), the A-RED inlet brine concentration, $C_{brine,IN}$, can be obtained by:

11

$$C_{brine,IN} = \frac{Q_{brine,RO}\, C_{brine,RO} + Q_{brine,F\&B}\, C_{brine,OUT}}{Q_{brine,RO} + Q_{brine,F\&B}} \tag{2}$$

where Q is the flow rate (m^3 s^{-1}), C is the molar concentration (mol m^{-3}), the subscript *brine* refers to the brine stream, the subscripts *IN* and *OUT* correspond to the inlet and outlet of the stack, while *RO* and *F&B* refer to streams arriving from the RO unit and from the feed & bleed recirculation loop, respectively.

The use of a feed & bleed loop on the permeate channel, as presented in Figure 3b, enables an increase in the concentration (and thus conductivity) of the inlet solution , $C_{perm,IN}$ (mol m^{-3}), according to the following *Eq. 2*:

$$C_{perm,IN} = \frac{Q_{perm,RO}\, C_{perm,RO} + Q_{perm,F\&B}\, C_{perm,OUT}}{Q_{perm,RO} + Q_{perm,F\&B}} \tag{3}$$

where the subscript *perm* refers to the permeate stream, while all remaining variables have been defined above.

Finally, the conductivity of the permeate after mixing with the bypass flow rate, as presented in Figure 3c and Figure 3d, can be obtained from the following equation:

$$C_{perm,target} = \frac{(Q_{perm,IN} - Q_{perm,F\&B})\, C_{perm,OUT} + Q_{perm,bypass}\, C_{perm,RO}}{Q_{perm,RO}} \tag{4}$$

where the subscript *perm,bypass* refers to bypassed permeate, while *perm,target* refers to the concentration of the total remineralized permeate obtained from the mixing of the stream exiting the A-RED stack with the permeate by-pass stream. Obviously, as in schemes a) and b) there is no permeate bypass loop, the A-RED system operates so that the outlet permeate conductivity coincides with the target conductivity values.

2.2.2 Parametric analysis for the identification of preferable operating conditions

Preliminary simulations were initially carried out with the simplest layout (Figure 3a) with only one feed & bleed loop for the brine. Subsequently, the feed & bleed loop for the permeate was added to the layout (as shown in Figure 3b) to increase permeate inlet salt concentration, thus reducing compartment resistance, and the two configurations were compared for the two remineralization targets (i.e. targets A and B).

From the results of these preliminary simulations, a larger simulation campaign was designed involving the more complex configuration of Figure 3c and Figure 3d for target A, which is the most challenging operating condition in terms of energy demand.

In all cases, independent operating parameters that were allowed to vary during the analysis were: i) applied voltage; ii) inlet permeate conductivity (depending on the recycled permeate flow rate); iii) RO permeate flow rate (affecting the permeate by-pass flow rate).

Table 3 shows the simulated conditions in terms of RO permeate, $Q_{perm,RO}$, and stack inlet conductivity (in $\mu S\ cm^{-1}$) of the permeate stream, while applied voltage was varied for each simulation in order to reach the desired permeate remineralization targets. A more detailed table is reported in Appendix C (Table C1).

Table 3. Operating conditions for the simulation campaign for the 4 schemes reported in Figure 3. Simulations were performed at a velocity of 10 cm s^{-1} along the stack (flow rate of 3.6 m^{3}h^{-1}) for both permeate and brine.

Scheme	$Q_{perm,RO}$ (m^3 h^{-1})	$Q_{brine,RO}$ (m^3 h^{-1})	$\sigma_{perm,IN}$ ($\mu S\ cm^{-1}$)	Target	I (A) and V (V)
Scheme 3a	3.6	0.6	10	A, B	
Scheme 3b	3	0.5	52	A	
	2.7	0.5	73	A	
	2.8	0.5	52	B	
	2.3	0.4	73	B	Adjusted to reach target outlet conductivity
Scheme 3c	3.4	0.6	10,70,100,130,160		
	4.5	0.8	10,70,100,130,160		
	5.7	1	10,70,100,130,160	A	
	8.5	1.5	10,70,100,130,160		
	14.2	2.5	10,70,100,130,160		
	19.8	3.5	10,70,100,130,160		
Scheme 3d	25.5	4.5*	10,70,100,130,160		
	31.2	5.5*	10,70,100,130,160	A	
	36.8	6.5*	10,70,100,130,160		
	42.5	7.5*	10,70,100,130,160		

*For these conditions only a fraction of the total $Q_{brine,RO,}$ equal to 3.6 m^3 h^{-1} was fed to the A-RED unit in order to guarantee the flow velocity of 10 cm s^{-1} in the stack. The amount of brine exceeding that value is imagined to be discarded or sent to further post-treatment steps.

2.3 Definition of technical performance parameters

In order to perform the simplified techno-economic analysis, two main technical performance indicators have been defined, namely the specific energy consumption and the apparent flux, according to the following definitions.

Specific Energy Consumption (SEC)

The main electric power consumption, $P_{Electric}$ (W), was related to the electrical consumption within the stack:

$$P_{Electric} = V * I \tag{5}$$

where V (V) is the external applied voltage to each stack, and I (A) is the sum of the electrical current in the two stacks. The external applied voltage takes into account the contribution of the voltage drop at the electrode compartments which was assumed equal to 5 V for industrial systems, as suggested by the stack manufacturer.

In addition, the power to pump solutions through the stacks, $P_{Pumping}$ (W), was calculated as:

$$P_{Pumping} = \frac{Q_{perm,IN}\,\Delta P_{perm} + Q_{brine,IN}\,\Delta P_{brine}}{\eta_{pump}} \tag{6}$$

where ΔP_{sol} (Pa) is the pressure loss in the stack and η_{pump} is the pump efficiency (assumed equal to 0.75).

With reference to Figure 3 schematics, the electric and pumping specific energy consumption per unit volume of remineralized permeate (*SEC_Electric* and *SEC_Pumping*) (kWh m^{-3}), were defined as:

$$SEC_{Electric} = \frac{10^{-3}\,P_{Electric}}{3,600\,Q_{perm,RO}} \tag{7}$$

$$SEC_{Pumping} = \frac{10^{-3}\,P_{Pumping}}{3,600\,Q_{perm,RO}} \tag{8}$$

The total specific energy consumption, SEC_{Tot} (kWh m^{-3}), was calculated as the sum of the two contributions as:

$$SEC_{Tot} = SEC_{Electric} + SEC_{Pumping} \tag{9}$$

14

The total specific energy consumption can be defined also with reference to the amount of recovered minerals, as the total power consumed per unit mass of salt transported from brine to permeate, SEC_s (kWh kg^{-1}), as follows:

$$SEC_{s,Tot} = SEC_{s,Electric} + SEC_{s,Pumping} \tag{10}$$

Where the meaning of symbols reflects the above definitions, while the subscript s indicates the normalisation with the mass of salts recovered. M_s is the salt molecular weight (g mol^{-1}).

$$SEC_{s,Electric} = \frac{P_{Electric}}{3,600\, M_s(Q_{perm,RO}C_{perm,target} - Q_{perm,RO}\, C_{perm,RO})} \tag{11}$$

$$SEC_{s,Pumping} = \frac{P_{Pumping}}{3,600\, M_s(Q_{perm,RO}C_{perm,target} - Q_{perm,RO}\, C_{perm,RO})} \tag{12}$$

Apparent Flux (J_{perm})

The apparent flux, J_{perm} (l h^{-1} m^{-2}), is defined as the ratio between the total remineralized permeate flow rate and the total membrane area of the two stacks:

$$J_{perm} = \frac{3.6 * 10^6\, Q_{perm,RO}}{2 * 2\, A\, n_{cp}} \tag{13}$$

where A (m^2) is the active area of each membrane in the stack.

2.4 Simplified economic model

The equations of the simplified economic model lead to the definition of the *total specific cost* (*TotC*) of remineralization, that can be defined as the sum of *operating specific costs* (*OpC*) and *capital specific costs* (*CapC*), expressed in € m^{-3} of remineralized permeate:

$$TotC = OpC + CapC \tag{14}$$

For the sake of simplicity, operating specific costs (OpC) were simply related to the major cost items of an electro-membrane process, this being the cost of energy consumed by the plant, calculated as:

$$OpC = SEC_{Tot}\, C_{Energy} \tag{15}$$

where C_{Energy} expresses the specific cost of electricity (in € (kWh)$^{-1}$).

Capital specific costs ($CapC$), conversely, were assumed to be proportional to the installed membrane area, via a lumped specific plant cost, as often reported in the literature for electro-membrane processes [50,51] as:

$$CapC = \frac{C_{Plant}}{J_{perm} \; x \; 10^{-3} \; t_{work} \; \tau_{plant}} \qquad (16)$$

where C_{Plant} is the cost of the plant, assumed proportional to membrane cost (in € m^{-2}), t_{work} are the number of operating hours in a year (assumed equal to 8000) and τ_{plant} is lifetime of the plant, assumed to be 5 years. The latter assumption allows to neglect the membrane replacement costs since it is reasonable to assume that the membranes have a lifetime of 5 years [52].

The input values used for the economic analysis are reported in Table 4: a reference case was first considered for the determination of the operating conditions guaranteeing the minimum *TotC*; also, *TotC* values were calculated (and compared) by varying energy and A-RED plant costs according to typical literature values [34,37,52,53].

Table 4. Cost assumptions for the economic analysis.

	Scenarios				
	Reference	2	3	4	5
Energy cost (€ (kWh) $^{-1}$)	0.1	0.05	0.2	0.05	0.2
A-RED plant cost (€ m^{-2})	125	50	50	200	200
A-RED plant lifetime (years) [34,52]	5				
Working hours per year [37]	8000				

3. RESULTS AND DISCUSSION

The simulation campaign has allowed to identify the influence of different operating conditions and selected configurations on the main technical performance indicators. In particular, using the basic configuration (as reported in Figure 3a) as baseline, the influence of the permeate recirculation (Figure 3b) and permeate by-pass flow rates (Figure 3c and Figure 3d) on the specific energy consumption is presented in the first two paragraphs, followed by results of the cost analysis for the different investigated scenarios.

3.1 Influence of the permeate recycle loop on the specific energy consumption

Table 5 reports the results for the basic case for which the standard scheme of Figure 3a is adopted, characterized by the presence of the feed & bleed loop only for the brine stream. In this case, the presence of a brine recirculation loop caused the inlet conductivity to decrease from $\cong 2990$ µS cm^{-1} to either $\cong 2020$ µS cm^{-1} or to $\cong 2320$ µS cm^{-1}, depending on the outlet permeate conductivity target (A or B targets corresponding to an outlet permeate conductivity of 260 µS cm^{-1} and 186 µS cm^{-1}, respectively). Notably, the desired target is achieved in both simulated cases, thus indicating that the basic configuration can already be used as a remineralisation stage for the RO permeate, although the high applied voltage (57 V and 49 V for target A and B respectively) and specific energy consumption (higher for the higher remineralization target, as expected) can be significantly optimized. This was mainly due to the very low conductivity of the inlet permeate, which resulted in a high resistance of the dilute compartment in the first part of the stack.

Table 5. Simulation results for the reference case adopting a brine feed & bleed loop configuration (Figure 3a).

FROM RO		IN A-RED			OUT A-RED		Electrical parameters		
$Q_{perm,RO}$ [m^3 h^{-1}]	$Q_{brine,RO}$ [m^3 h^{-1}]	$Q_{brine,F\&B}$ [m^3 h^{-1}]	$\sigma_{perm,IN}$ [µS cm^{-1}]	$\sigma_{brine,IN}$ [µS cm^{-1}]	Target	$\sigma_{brine,OUT}$ [µS cm^{-1}]	V [V]	I [A]	SEC_{Tot} [kWh m^{-3}]
3.6	0.6	3	10	2017	A	1784	57	3.9	0.20
3.6	0.6	3	10	2322	B	2163	49	2.8	0.17

The scheme proposed in Figure 3b allows for the increase of inlet permeate conductivity by implementing recycling of the outlet permeate, which has a much higher conductivity than the inlet permeate. Thus, the influence of a different inlet conductivity, obtained by varying the percentage of recycled permeate, on the specific energy consumption was reported in Figure 4 for the two permeate conductivity targets A and B.

Starting from the A target simulations ($\sigma_{perm,target} = 260$ µS cm^{-1}), the electric contribution to the SEC_s (i.e. $SEC_{s,Electric}$) decreased from ~0.28 kWh kg^{-1} to ~0.10 kWh kg^{-1}, when the inlet conductivity increased from 10 µS cm^{-1} (no permeate feed & bleed, i.e. scheme a) of Figure 3) to 73 µS cm^{-1} (25% of outlet permeate recycled to the inlet of the stack). Similarly, for the B target simulations ($\sigma_{perm,target} = 186$ µS cm^{-1}), the $SEC_{s,Electric}$ was reduced from ~0.25 kWh kg^{-1} to ~0.06 kWh kg^{-1} when the outlet permeate recycled to the entrance increased from 0% (or $\sigma_{perm,IN} = 10$ µS cm^{-1}) to 36% (or $\sigma_{perm,IN} = 73$ µS cm^{-1}). It is worth noting that the production capacity of the system for the A target was slightly

17

larger than that obtained at B target (see Table 3), as the higher outlet conductivity leads to lower required recirculation rate.

Pumping power, $P_{Pumping}$, was calculated by *eq. 6* as a function of flow rate with pressure drop estimated by the model being ≈ 1.7 bar for the two stacks in series. Although the pumping power is approximately constant as the permeate inlet conductivity increased, both pumping SEC_s and SEC (being normalized quantities) increased as the permeate recirculation rate increased. Thus, $SEC_{s,Pumping}$ rose with inlet conductivity and was higher for target B due to the lower salt recovery, ranging between $\cong 0.77$-1.21 kWh kg^{-1} versus $\cong 0.53$-0.71 kWh kg^{-1} for target A.

Summing electrical and pumping energy consumptions lead to the $SEC_{s,Tot}$, which remained approximately constant at $\cong 0.8$ kWh kg^{-1} for target A, while it increased by 25% from an initial value of $\cong 1$ kWh kg^{-1} for target B as inlet permeate conductivity increased.

Similar trends can be observed also for the specific energy consumption normalised by the volume of remineralized permeate, *SEC*, (see Figure 4b). In particular, SEC_{Tot} was equal to $\cong 0.19$ kWh m^{-3} for target A, while it increased from 0.17 kWh m^{-3} to 0.21 kWh m^{-3} for target B.
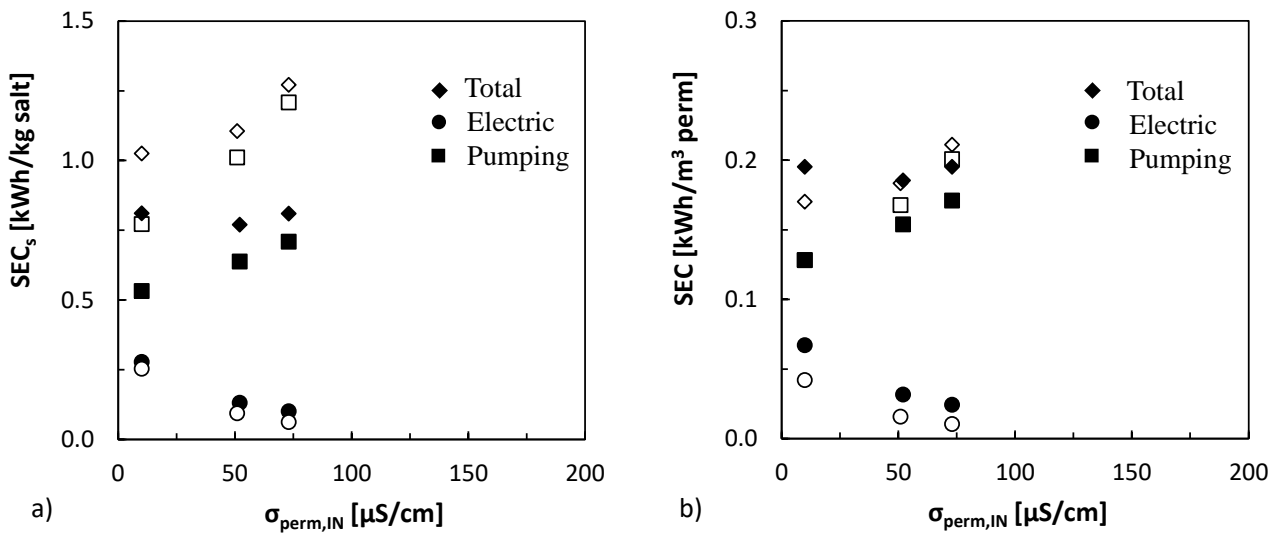
Figure 4. Specific energy consumption per kg of salt (a) and m^3 of remineralised permeate (b), as a function of inlet permeate conductivity for configurations 3a/3b. Permeate conductivity target A = 260 µS cm^{-1} (full symbols), target B = 186 µS cm^{-1} (empty symbols).

In conclusion, for configuration 3b, the advantage of lowering the electrical consumption by recycling part of the permeate was fully counterbalanced by the increase in pumping consumption due to the recycle loop, thus significantly limiting the benefits of this scheme.

Such limitation can be overcome by adding a permeate by-pass stream (scheme 3c), as better detailed in the next sub-section.

3.2 Influence of the permeate bypass on the specific energy consumption

Simulations of scheme 3c were performed by varying the inlet permeate conductivity. Results were compared at fixed values of production capacity, $Q_{perm,RO}$, ranging from 3.6 to 42 m^3 h^{-1}. Thus, in order to meet the $Q_{perm,RO}$, the increase of permeate recycled flow rate, $Q_{perm,F\&B}$, was compensated by a higher bypassed flow rate $Q_{perm,bypass}$ (see Figure 3c).

For the sake of brevity, only the *SEC* per volume of remineralized permeate are presented (Figure 5) as a function of inlet permeate conductivity, referring to the case of target A (260 µS cm^{-1}). In particular, Figure 5a shows both the $SEC_{Electric}$ and the $SEC_{Pumping}$, while Figure 5b reports the SEC_{Tot}.

In these cases, when the inlet conductivity increased from 10 µS cm^{-1} to 70 µS cm^{-1}, the electric specific energy consumption, $SEC_{Electric}$, was significantly reduced from ≈0.19 kWh m^{-3} to ≈0.15 kWh m^{-3} in the case of maximum permeate flow rate (42.5 m^3 h^{-1}) by recirculating 2% of the outlet permeate flow rate, while it was reduced from ≈0.07 kWh m^{-3} to ≈0.04 kWh m^{-3} in the case of 4.5 m^3 h^{-1} when 16% of the outlet permeate flowrate was recycled. That effect was due to a higher inlet permeate conductivity in this latter case, which reduced the total stack resistance [52,54]. This benefit was significantly dampened when the inlet conductivity was further increased from 70 µS cm^{-1} to 160 µS cm^{-1}.

It is worth noting that, in some cases (e.g. with very low inlet conductivity and high permeate flow rate), remineralisation could be achieved only by applying a voltage higher than the recommended value of 1 ΔV/cell pair (indicated by triangular symbols on the graph). In these cases, the permeate recirculation acted as a very effective strategy to allow operation at much lower applied voltage, leading also to the benefit of lower $SEC_{Electric}$. For example, at a remineralized flow rate of 19.8 m^3 h^{-1}, the applied voltage was reduced from 103 V to 65 V and 51 V, when the inlet conductivity increased from 10 µS cm^{-1} to 70 µS cm^{-1} and 160 µS cm^{-1}, respectively. For the same reason, at production capacity of 25.5 m^3 h^{-1}, the plant could operate only if the permeate recirculation rate was large enough to ensure an increase in the inlet conductivity in the range of 100-160 µS cm^{-1}. That condition resulted in a corresponding applied voltage in the range of 62-69 V, decreasing with $\sigma_{perm,IN}$.

On the other hand, for each inlet conductivity, $SEC_{Electric}$ increased with the remineralized flow rate due to the larger amount of salt to be transported to meet the target conductivity, with consequent

higher applied voltage and currents. Notably, at permeate flow rates above 19.8 m³ h⁻¹, the brine arriving from the RO is sufficient to feed the A-RED unit without the need for a recycle loop. This leads to a limitation in the amount of salt carried by the inlet brine, which contributes to the much steeper increase in the $SEC_{Electric}$.

The pumping power is independent of the by-pass permeate stream. For this reason, a significant reduction of $SEC_{Pumping}$ was observed when the total plant capacity (remineralised permeate flow rate) increased: $SEC_{Pumping}$ decreased from ≈0.14 kWh m⁻³ to ≈0.01 kWh m⁻³ when the remineralized permeate flow rate increased from 3.4 m³ h⁻¹ to 42.5 m³ h⁻¹. It became a negligible fraction of the SEC_{Tot} only for large capacities while it remained a significant fraction of the SEC_{Tot} for low-medium plant production, as already observed in the case of brackish water ED desalination [52]. $SEC_{Pumping}$ were higher than $SEC_{Electric}$ for production capacities below or equal to 4.5 m³ h⁻¹, for any inlet permeate conductivity value. In the case of 5.7 m³ h⁻¹, $SEC_{Pumping}$ were 1-2.7 times larger than $SEC_{Electric}$ while they were always lower than $SEC_{Electric}$ for capacities of at least 14.2 m³ h⁻¹.

Due to the different trends of $SEC_{Electric}$ and $SEC_{Pumping}$ as function of the plant capacity, the total specific energy consumption, SEC_{Tot}, (see Figure 5b) exhibited a minimum around a flow rate of ≈14 m³ h⁻¹ (0.15 m³ h⁻¹ m⁻²$_{installed-IEM-area}$), corresponding to a value of 0.08 kWh m⁻³ for the largest inlet conductivity of 160 µS cm⁻¹.

It is worth noting that, at equivalent permeate flow rate, a minimum was observed also for the 10 µS cm⁻¹ inlet conductivity but corresponding to a much higher SEC_{Tot} of 0.14 kWh m⁻³.
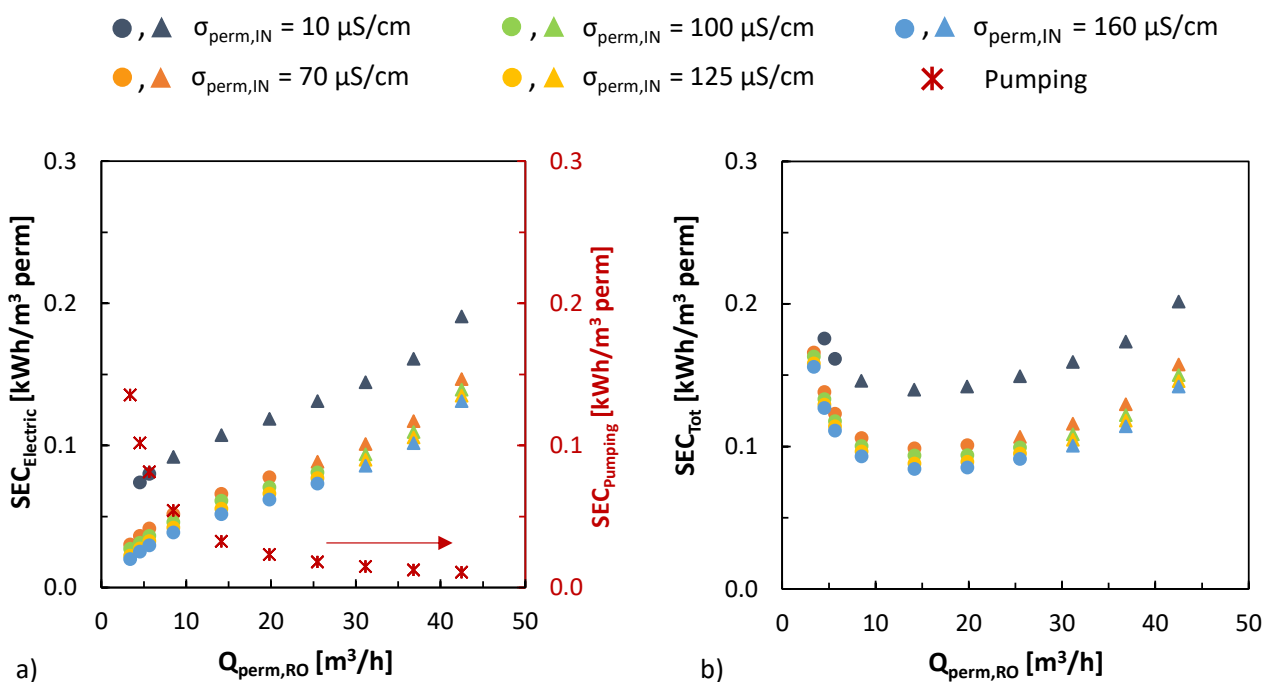
Figure 5. Specific energy consumption per m³ of remineralized permeate as a function of total production capacities and for different inlet permeate conductivities ranging from 10 µS cm⁻¹ to 160 µS cm⁻¹. a) Electric and pumping specific energy consumptions; b) total specific energy consumption. Simulations referred to a permeate target conductivity of 260 µS cm⁻¹ (target A) and a flow velocity of 10 cm s⁻¹. Triangle symbols represented conditions that cannot be operated at due to an applied potential exceeding the maximum allowed by the manufacturers (1 ΔV/CP).

3.3 *Influence of operating conditions and process configuration on remineralization costs*

A cost analysis has been performed for all scenarios already described, highlighting the effects of different operating conditions and process layout on the specific operating and capital costs. For the sake of brevity, only results referring to the remineralisation target of 260 µS cm⁻¹ (target A) are presented in Figure 6, this condition being the most challenging in terms of energy consumption and membrane area requirements.

As detailed above, remineralisation operating specific costs were assumed to be directly proportional to the SEC_{Tot}. Thus, they decreased when increasing the remineralized flow rate until reaching a minimum of around 14 m³ h⁻¹, after which the costs increased for higher flow rates. Operating costs (around the "optimal" flow rate) were reduced up to 30% when the inlet conductivity was increased from 10 µS cm⁻¹ to 70 µS cm⁻¹, while a further increase in the inlet permeate conductivity (thus in the permeate recirculation flow rate) had a minor effect on operating specific cost. Overall, *OpC* varied from a minimum of ≈0.84 c€ m⁻³ for a capacity of ≈14 m³ h⁻¹ and maximum recirculation rate to a maximum of ≈2.02 c€ m⁻³ observed in our analysis with high remineralised flow rate and no permeate recycle.

Concerning capital costs, calculated as a function of installed membrane area and including the costs for equipment, they varied between 8.6 c€ m⁻³ and 0.7 c€ m⁻³, always decreasing with the increase of the apparent flux (see eq. 16), i.e. with the increase of the remineralized flow rate. For the simulation carried out at minimum permeate flow rate and inlet conductivity, the capital costs were about 5 times larger than the operating costs (8.6 c€ m⁻³ and 1.84 c€ m⁻³, respectively), whereas, as the flow rate increased, the difference was reduced until it became comparable at average flow rates. At the maximum analysed capacity, the capital costs reached values 2-3 times lower than operating costs. It is important to note that capital costs were reduced by almost 90% by implementing a permeate bypass configuration that leads to much higher remineralised flow rate.

Obviously, in order to match the final conductivity target after mixing with the by-pass stream, the outlet permeate will need to reach a much higher conductivity, which requires to keep low electrical resistance in the stacks through application of the permeate recycle-loop. When applying this scheme, the very high outlet conductivity (up to 1.50 - 2.95 mS cm^{-1} in some cases) facilitates the increase of inlet conductivity while requiring low recycle rates of the permeate. Another advantage of processing high permeate flow rates was the increase in the corresponding brine flow rate available from the RO unit. This makes it possible to reduce or eliminate the brine recirculation flow rate. Capital costs could be further reduced by increasing the system capacity ($Q_{perm,RO}$ in the range of $31 - 43$ m^3 h^{-1}), though these conditions require an applied voltage higher than the maximum recommended value (triangular symbols in Figure 6).
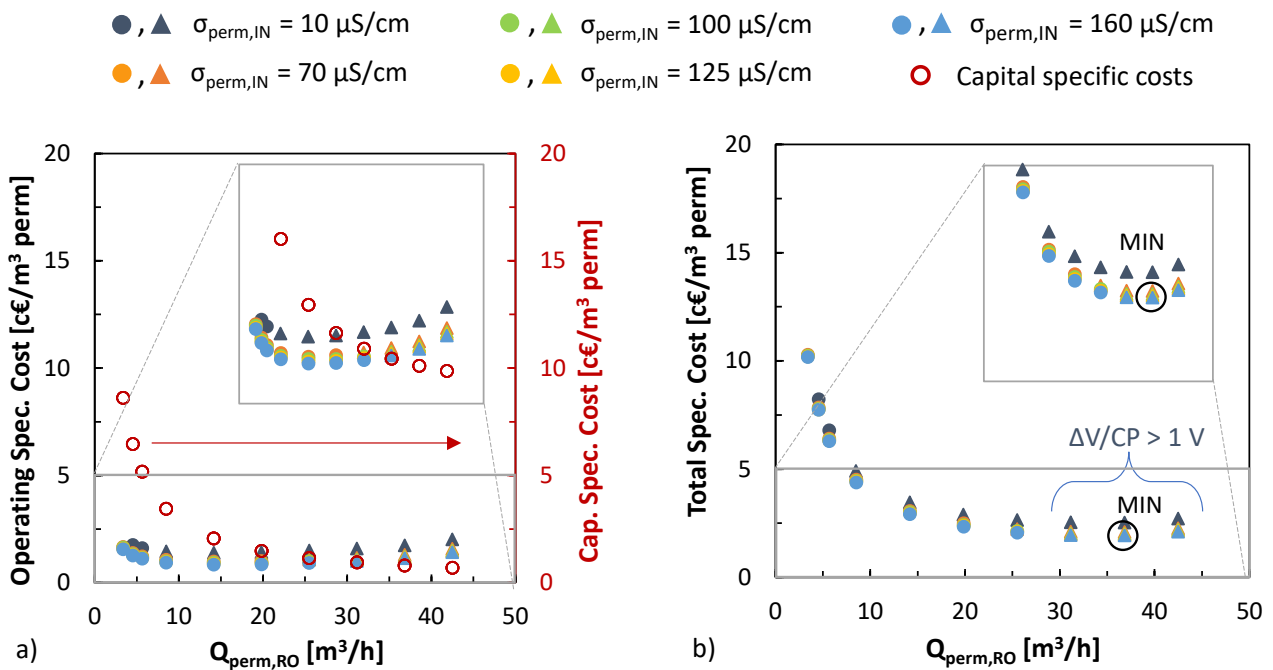
Figure 6. Remineralization costs as a function of remineralized permeate flow rate for inlet permeate conductivities varying from 10 µS cm^{-1} to 160 µS cm^{-1}. a) Operating and Capital specific costs; b) Total specific costs. Permeate conductivity target A (260 µS cm^{-1}), channel velocity = 10 cm s^{-1}. Triangle symbols represent conditions requiring an applied potential exceeding the one suggested by the manufacturer (1 ∆V/CP).

Figure 6b shows the total costs per m^3 of remineralized permeate as a function of production capacity ($Q_{perm,RO}$) and inlet permeate conductivity. *TotC* varies from about 10 c€ m^{-3} to less than 2 c€ m^{-3} for a remineralized flow rate of 37 m^3 h^{-1}, although this condition requires an applied voltage above the manufacturer's operating limit. Limiting the analysis to the technically feasible range of applied voltage, the minimum total cost of 2.1 c€ m^{-3} can be obtained for a capacity of ≈ 26 m^3 h^{-1} (0.27 m^3 h^{-1} m^{-2}$_{installed-IEM-area}$) of which $\approx 87\%$ is bypassed, with $\approx 8\%$ of permeate recirculation to increase inlet conductivity to 160 µS cm^{-1}.

Figure 7 shows the comparison for SEC and specific costs for the three different schemes of Figure 3. These results referred to target A and an inlet permeate conductivity of 70 µS cm^{-1} for schemes b) and c). As noted in section 3.1, the addition of the feed & bleed loop for permeate (scheme b) did not lead to a reduction in SEC_{Tot} since the reduction in the electrical contribution was offset by an increase in the energy contribution related to pumping. Indeed, the total cost increased by 27%, as a consequence of the increase in specific capital costs, since the total remineralised permeate was reduced. The addition of a permeate bypass, i.e. the increase in the capacity of the system, provided significant benefits in terms of both reduced SEC_{Tot} (and OpC) and lower $CapC$. In fact, $TotC$ were more than 5 times lower when the permeate bypass was included.
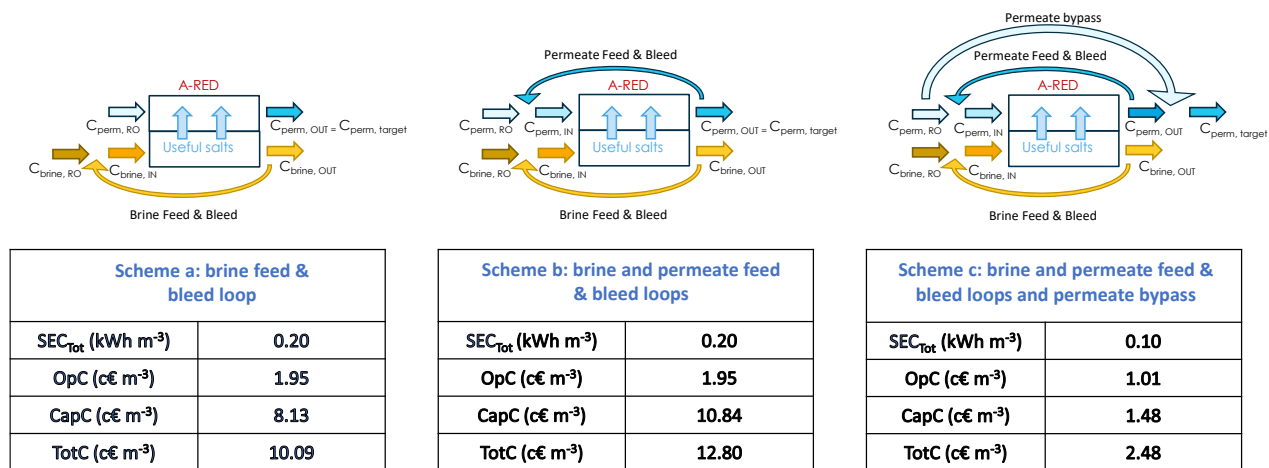

Scheme a: brine feed & bleed loop	
SEC$_{Tot}$ (kWh m^{-3})	0.20
OpC (c€ m^{-3})	1.95
CapC (c€ m^{-3})	8.13
TotC (c€ m^{-3})	10.09

Scheme b: brine and permeate feed & bleed loops	
SEC$_{Tot}$ (kWh m^{-3})	0.20
OpC (c€ m^{-3})	1.95
CapC (c€ m^{-3})	10.84
TotC (c€ m^{-3})	12.80

Scheme c: brine and permeate feed & bleed loops and permeate bypass	
SEC$_{Tot}$ (kWh m^{-3})	0.10
OpC (c€ m^{-3})	1.01
CapC (c€ m^{-3})	1.48
TotC (c€ m^{-3})	2.48

Figure 7. Comparison of SEC (kWh m^{-3}) and specific costs (OpC, CapC and TotC in c€ m^{-3}) for schemes a with only brine feed & bleed loop, b) brine and permeate feed & bleed loops and c) brine and permeate feed & bleed loops and permeate bypass. The comparison was performed considering an inlet permeate conductivity of 70 µS cm^{-1} for schemes b and c and target A.

3.4 Influence of membrane and energy costs on remineralization costs

The economic analysis was completed also considering a parametric study of the influence of membrane and energy costs on the total cost of the remineralisation process. Four extreme conditions were analysed, with energy cost ranging from 0.05 to 0.2 € (kWh)$^{-1}$ and A-RED capital cost ranging from 50 to 200 € m^{-2} of overall (AEM + CEM) installed active membrane area (Table 4). Results are reported in Figure 8, again for the sole case of target A.

Apart from the expected result that higher energy and plant costs led to higher remineralization costs, the analysis indicated how the optimal conditions minimising overall cost significantly shift when changing energy and plant specific costs.

The minimum cost obtained ranged between 0.88-3.51 c€ m^{-3} (Figure 8a) while the maximum cost ranged from 3.51 to 17.46 c€ m^{-3} (Figure 8d). In addition, the increase of plant cost (from 50 to 200 € m^{-2}) resulted in larger remineralised flow rates minimising the *TotC* (Figure 8b), though this was still more than double that of the case at lowest plant costs (1.8 c€ m^{-3} against 0.88 c€ m^{-3}). On the other hand, the increase in energy cost (from 0.05 to 0.20 € (kWh)$^{-1}$) resulted in a greater benefit of using permeate recycling, thus obtaining a minimum cost at a remineralised flow rate around $\approx$26 m^3 h^{-1} (or 0.27 m^3 h^{-1} m$^{-2}_{\text{installed-IEM-area}}$), as observed in Figure 8c. However, it is important to note that in most cases the minimum cost condition was obtained with an applied voltage greater than 1 ΔV/CP, a limiting condition suggested by the membrane manufacturer. This is not the case for Figure 8c where the minimum cost condition was achieved under a feasible voltage value (i.e. < 1 ΔV/CP). This condition corresponds to an output of $\approx$26 m^3 h^{-1} and permeate inlet conductivity of 100-160 μS cm^{-1}. When applying these optimal feasible operating conditions, the effect of changing the energy and A-RED plant costs resulted in a cost variation in the range of 0.9-3.7 c€ m^{-3} with respect to the cost of 2.1 c€ m^{-3}obtained under standard operating conditions (Figure 6).
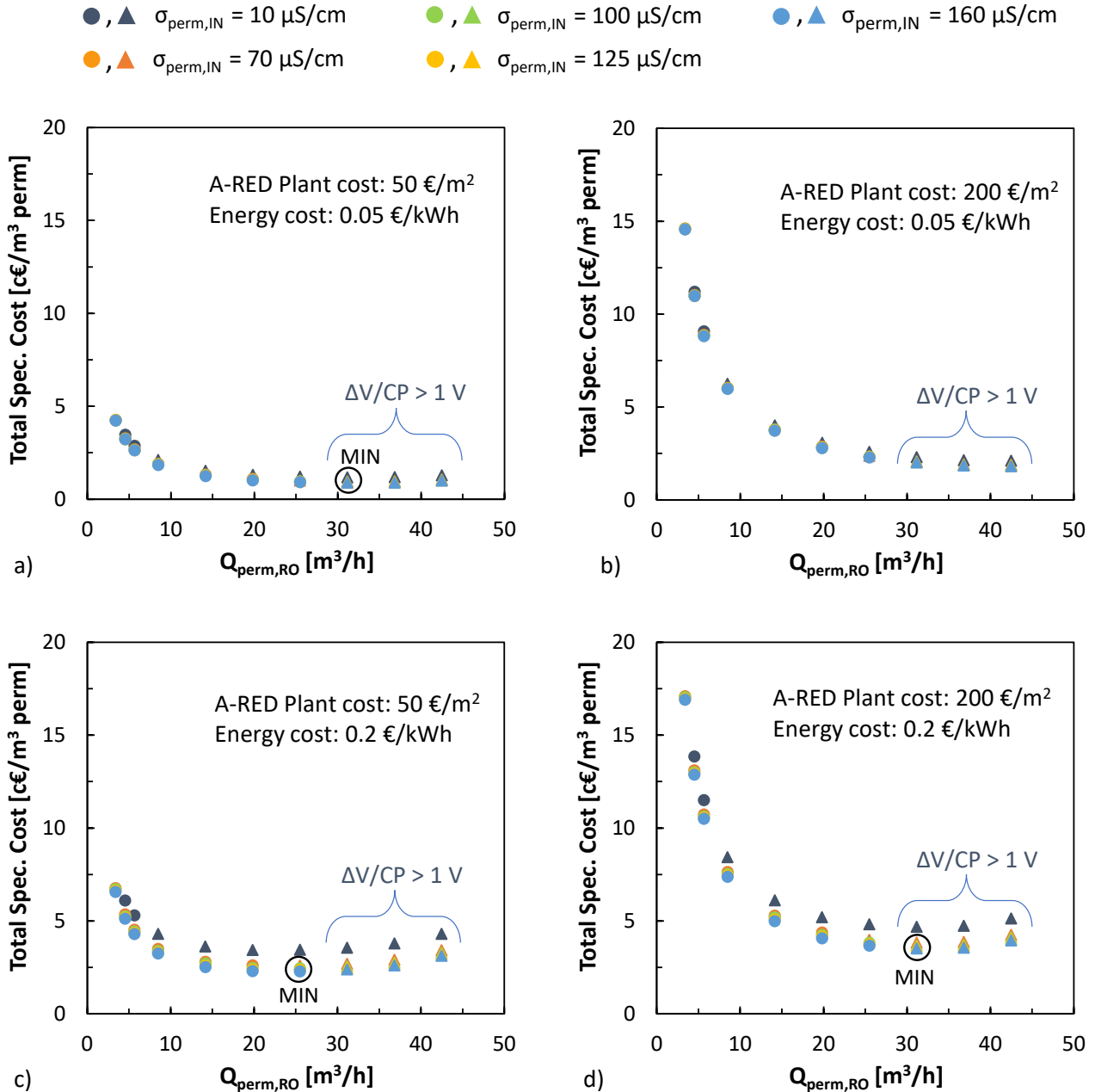
Figure 8. Remineralization cost as a function of remineralized permeate flow rate and with variable permeate inlet conductivity (10 - 160 μS cm⁻¹) in four different cost scenarios. a) A-RED cost = 50 € m⁻², energy cost = 0.05 € (kWh)⁻¹; b) A-RED cost of 200 € m⁻² and electricity cost of 0.05 €(kWh)⁻¹; c) A-RED cost of 50 € m⁻² and electricity cost of 0.2 € (kWh)⁻¹; d) A-RED cost of 200 € m⁻² and electricity cost of 0.2 € (kWh)⁻¹. Target permeate conductivity of 260 μS cm⁻¹ (target A) and channel velocity of 10 cm s⁻¹. Triangle symbols represent conditions requiring an applied potential exceeding the one suggested by the manufacturer (1 ΔV/CP).

It is worth noting that both specific energy consumption and specific costs are normalised for the production capacities of the plant, thus are directly scalable to fully industrial scale plants, as long as the following quantities are kept constant: (i) recirculation and bypass percentages, (ii) RO outlet

stream conductivities and (iii) final permeate target. Notably, the detrimental phenomenon of voltage drop at the electrodic compartments, fixed at 5V, is known to be negligible for industrial scale stacks and it does not play a crucial role at the pilot scale as: (i) for high permeate production rates, high applied voltages are adopted, while (ii) for low permeate production rates, SEC_{Tot} is mainly affected by $SEC_{Pumping}$. In fact, simulations performed with 500 cell pairs (not shown here for the sake of brevity) exhibited a SEC_{Tot} difference from the corresponding pilot-scale always below 3%.

Overall, the analysis presents very promising results when compared to the typical costs of RO permeate post-treatment, especially when considering that ion exchange membrane and equipment costs are expected to reduce in the coming years. Table 6**Table 6** reports the comparison among *TotC* reported in literature for conventional and emerging remineralization processes. As can be seen, adopting A-RED as a remineralization step may guarantee the lowest cost. Clearly, the planned experimental campaign at pilot scale including long-run tests will provide essential information to confirm such an outcome.

Table 6. Cost comparison for desalinated water remineralization process.

Type of remineralization process	Scale plant	Total remineralization cost	Reference
Lime/carbon dioxide	100000 $m^3 day^{-1}$	5.8 US \$cent m^{-3}	[22,55]
H_2SO_4 + based calcite dissolution	Pilot plant	4.9 – 5.4 \$cent m^{-3}	[24]
Acetic acid + calcite dissolution + UV treatment	Small scale	6.4 \$cent m^{-3}	[25]
Lim saturator	13000 $m^3 day^{-1}$	6.5 c€ m^{-3}	[23]
Caustic soda	13000 $m^3 day^{-1}$	3.9 c€ m^{-3}	[23]
A-RED process	Industrial plant	0.9 – 3.7 c€ m^{-3}	This work

CONCLUSIONS

An innovative use of Assisted-Reverse Electrodialysis has been proposed for the remineralization of surface water RO permeate by recovering the minerals already contained in the RO brine. The proposed technology relies on the fact that all the salts required for remineralization are already present in the brine coming from the same plant. The use of an electro-membrane process for their recovery represents a more sustainable alternative to the use of chemicals.

An A-RED model was re-adapted, validated with experimental data and used to analyse the system performance in several configurations and operating conditions for a commercial industrial unit (SUEZ-WTS). Simulations of different process layouts were performed, including: (i) simple feed & bleed loop for brine stream; (ii) addition of feed & bleed loop for the permeate stream; (iii) addition of permeate bypass loop to increase the system production capacity.

Results confirmed the feasibility of the new proposed process for the remineralization of RO permeate. In particular, complying with current manufacturer recommendations (i.e. max 1 ΔV/cell pair), a permeate flow rate up to 0.27 m^3 h^{-1} $m^{-2}_{installed-IEM-area}$ can be remineralized by increasing its conductivity from 10 μS cm^{-1} to 260 μS cm^{-1} (corresponding to a hardness of 13°f or 130 mg l^{-1} as $CaCO_3$).

The minimum specific energy consumption (SEC_{Tot}) was obtained for productivity of $\approx$0.15 m^3 h^{-1} $m^{-2}_{installed-IEM-area}$ which, interestingly, was not dependent on the recirculation permeate flow rate (at least within the operating conditions simulated here). Moreover, the simple, yet original, adoption of a combined use of permeate bypass and feed & bleed loops, and the corresponding increase from 10 μS cm^{-1} to 160 μS cm^{-1} in the inlet permeate conductivity, allowed the reduction of the minimum SEC_{Tot} from 0.14 kWh m^{-3} down to 0.08 kWh m^{-3}.

An economic feasibility analysis was also performed and different scenarios were investigated. For the reference case, the optimal operating conditions corresponded to a specific total cost ($TotC$) of 2.1 c€ m^{-3}. The techno-economic analysis was extended by varying the plant and energy costs within a realistic range (i.e. 0.05-0.2 € $(kWh)^{-1}$ and 50-200 € $m^{-2}_{installed-IEM-area}$) in order to study their impact on $TotC$. Simulations provided a corresponding $TotC$ ranging from 0.9 to 3.7 c€ m^{-3}. All these values were lower than those relevant to conventional and emerging remineralization technologies, thereby representing an encouraging result for a future industrial implementation of the process.

Next steps will include an experimental campaign at the pilot scale and a feasibility analysis for brines with different features and composition.

NOMENCLATURE

Acronyms

AEM	Anionic Exchange membrane
A-RED	Assisted-Reverse Electrodialysis
CEM	Cationic Exchange membrane
CP	Cell pair
ED	Electrodialysis
IEM	Ionic Exchange membrane
OCV	Open Circuit Voltage
RO	Reverse Osmosis

RED   Reverse Electrodialysis

Symbols

A	Active membrane area (m^2)
B	Width (m)
C	Molar concentration (mol m^{-3})
C_{Energy}	Energy cost (€ $(kWh)^{-1}$)
C_{plant}	A-RED Plant Cost (€ m^{-2})
$CapC$	Capital cost (€ m^{-3})
D	Salt diffusivity (m^2 s^{-1})
E	Electro-motive force (V)
F	Faraday constant (C mol^{-1})
f	Darcy friction coefficient (-)
f_s	Shadow factor (-)
G	Mass flow rate (kg s^{-1})
I	Current (A)
i	Current density (A m^{-2})
J_{perm}	Apparent flux (l h^{-1} m^{-2})
J_w	Water flux (m^3 s^{-1} m^{-2})
L^{IEM}	IEM osmotic permeability (m^3 Pa^{-1} m^{-2} s^{-1})
M	Salt Molecular weight (g mol^{-1})
M_w	Water Molecular weight (g mol^{-1})
N_s	Salt molar flux (mol s^{-1} m^{-2})
n_{cp}	Number of cell pairs (-)
n_H	Hydration number (-)
OpC	Operating cost (€ m^{-3})
P	Consumed power for two stacks (W)
Q	Flow rate (m^3 s^{-1})
R	Gas constant (J mol^{-1} K^{-1})
r	Areal resistance (Ω m^2)
SEC	Specific energy consumption per m^3 of permeate (kWh m^{-3})
SEC_s	Specific energy consumption per kg of transported salt (kWh kg^{-1})
T	Absolute temperature (K)
t_{work}	working hours per year (h y^{-1})
$TotC$	Total cost (€ m^{-3})
u	Velocity (m s^{-1})
V	Voltage (V)
y	Main flow direction in the channel (m)
z	charge number of the generic ion (-)

Greek symbols

α	Perm-selectivity (-)
δ	Thickness (m)
ΔP	Pressure loss (Pa)
ΔV_{ext}	External applied Voltage (V)
γ	Activity coefficient (-)
η	Efficiency (-)
η_{BL}	Non-Ohmic voltage drop (V)
π	Osmotic pressure (Pa)
ρ	Water density (kg m^{-3})

σ Conductivity (S m^{-1})

τ_{plant} Plant life (year)

Subscripts

AEM	Anionic Exchange membrane
Bypass	Bypass stream
Brine	Brine stream
CEM	Cationic Exchange membrane
Diff	Diffusive
Electr-osm	Electro-osmotic
Electric	Electric energy to power the stack
Ext	External
F&B	Feed & bleed stream
H	Hydratation
IEM	Ionic exchange membrane
IN	Inlet of the stack
Int	Interface
Migr	Migrative
Ω	Ohmic
OSM	Osmotic
OUT	Outlet of the stack
Perm	Permeate stream
Pump	Pump
Pumping	Pumping energy related to pressure losses
RO	Reference
Ref	Stream generated by reverse osmosis pilot
s	salt
SOL	Generic solution
Target	Target conductivity
Tot	Total
w	Water

Appendix

Appendix A. Model equations

Transport phenomena and mass balances

The mass balances of salt in the generic interval, along the main flow direction in the channel (i.e. *y*), are expressed as:

$$-\frac{dG_{brine,s}(y)}{dy} = \frac{dG_{perm,s}(y)}{dy} = 10^{-3} M_s \, b \, N_s(y) \qquad (A\ 1)$$

where $G_{SOL,S}$ (kg s^{-1}) is the salt mass flow rate of the generic solution, *brine* and *perm* clearly indicate the brine and permeate, M_s (g mol^{-1}) is the molar mass of NaHCO$_3$ salt, *b* (m) is the stack width. N_s (mol m^{-2} s^{-1}) is the molar flux of salt, composed by two terms: the migration flux, N_s^{migr} , and the diffusive one, N_s^{diff}:

$$N_s(y) = N_s^{migr}(y) + N_s^{diff}(y) \qquad (A\ 2)17$$

For monovalent ions, the migration flux is proportional to the ion current density, *i* (A m^{-2}), as reported in the following expression:

$$N_s^{migr}(y) = \frac{i(y)}{zF} \qquad (A\ 3)$$

where *F* (C mol^{-1}) is the Faraday constant, z is the valence (equal to 1 in our case where bicarbonate and sodium ions are studied).

The diffusive flux can be written as the sum of the diffusive fluxes through the two *IEMs*, respectively *CEM* and *AEM*:

$$N_s^{diff}(y) = N_{s,CEM}^{diff}(y) + N_{s,AEM}^{diff}(y) = \frac{D^{CEM}(C_{brine}^{CEM,int}(y) - C_{perm}^{CEM,int}(y))}{\delta_{CEM}} + \frac{D^{AEM}(C_{brine}^{AEM,int}(y) - C_{perm}^{AEM,int}(y))}{\delta_{AEM}} \qquad (A\ 4)$$

where D^{IEM} is the salt diffusivity in the ion exchange membrane (assumed equal to 4*e^{-12} m^2 s^{-1} [44]), $C_{sol}^{IEM,int}$ is the generic concentration at the solution-membrane interface (mol m^{-3}), calculated as a function of the polarization coefficients and bulk concentrations as done in [37], δ_{IEM} (m) is the membrane thickness.

The mass balances of water along the channel can be written as:

$$\frac{dG_{brine,w}(y)}{dy} = -\frac{dG_{perm,w}(y)}{dy} = \rho_w J_w(y)b \qquad (A\,5)$$

in which $G_{SOL,w}$ (kg s^{-1}) is the water mass flow rate, ρ_w (kg m^{-3}) is the water density and J_w (m^3 m^{-2} s^{-1}) is the overall trans-membrane water flux, given by the difference between the osmotic flux, $J_{w,OSM}$ (m^3 m^{-2} s^{-1}), and electro-osmotic flux, $J_{w,Elect-OSM}$ (m^3 m^{-2} s^{-1}):

$$J_w(y) = J_{w,OSM}(y) - J_{w,Elect-OSM}(y) \qquad (A\,6)$$

The osmotic flux is directed from the diluate to the concentrate stream, so from the permeate to the brine, and can be expressed as:

$$J_{w,OSM}(y) = L^{CEM}\left(\pi_{brine}^{CEM,int}(y) - \pi_{perm}^{CEM,int}(y)\right) + L^{AEM}\left(\pi_{brine}^{AEM,int}(y) - \pi_{perm}^{AEM,int}(y)\right) \quad (A\,7)$$

where L^{IEM} (m^3 Pa^{-1} s^{-1} m^{-2}) is the osmotic permeability of the generic membrane (assumed equal to 4 ml m^{-2} bar^{-1} h [44,56]) and $\pi_{SOL}^{IEM,int}$ (Pa) is the osmotic pressure corresponding to the concentration at the generic membrane-solution interface, calculated by Pitzer's correlations [57].

The electro-osmosis transport mechanism is attributed to the water flux coupled to the ion flux because of the water molecules of the solvation shell and it is calculated as a function of the overall salt flux:

$$J_{w,Elect-OSM}(y) = n_H N_s(y)\frac{M_w}{\rho_w}10^{-3} \qquad (A\,818)$$

in which n_H (-) is the hydration number (set equal to 7 [58]) and M_w (g mol^{-1}) is the molar mass of water.

Electric variables and concentration polarization

The current flowing in the stack is a function of the applied voltage and the cell pair potential. For monovalent ions, the open circuit voltage (OCV) can be given by Nernst's equation:

$$OCV = (\alpha_{CEM} + \alpha_{AEM})\frac{RT}{F}\ln\left[\frac{\gamma_{brine,IN}\,C_{brine,IN}}{\gamma_{perm,IN}\,C_{perm,IN}}\right] \qquad (A\,919)$$

where $\alpha_{IEM}(-)$ is the perm-selectivity of the generic membrane *IEM* (see Table 1), $\gamma_{SOL,IN}$ and $C_{SOL,IN}$ are the activity coefficient and the concentration of the generic solution at the inlet of the stack, respectively. R (J mol^{-1} K^{-1}) and T (K) are the gas constant and the absolute temperature. Activity coefficient can be estimated through Pitzer's correlation as a function of the concentrations [59]. Since the concentration difference between permeate and brine decreases along the y direction in the stack due to the mass transport, it is more suitable to adopt the local electro-motive force, E, which is function of the local concentration $C_{SOL}(y)$:

$$E(y) = (\alpha_{CEM} + \alpha_{AEM})\frac{RT}{F} \ln \left[\frac{\gamma_{brine}(y)C_{brine}(y)}{\gamma_{perm}(y)C_{perm}(y)} \right] \qquad (A\ 10)$$

The local current density, i, can be written as:

$$i\ (y) = \frac{\Delta V_{ext} - E(y) - \eta_{BL}(y)}{r_\Omega(y)} \qquad (A\ 1120)$$

where ΔV_{ext} (V) is the external applied voltage, η_{BL} (V) is the non-Ohmic voltage drop due to concentration polarization, estimated by polarization coefficients deriving from Sherwood number correlations obtained from CFD simulations [44]. r_Ω (Ω m^2) is the areal Ohmic resistances of the cell pair. The electrode voltage drop was assumed to be equal to 5V, as suggested by manufacturer for the plant scale.

The cell pair resistance, r_Ω , can be calculated as the sum of membranes and compartments resistances, r_{IEM} (Ω m^2) and r_{SOL}(Ω m^2).

$$r_\Omega\ (y) = r_{CEM}(y) + r_{AEM}(y) + r_{perm}(y) + r_{brine}(y) \qquad (A\ 12)$$

The channel resistances (r_{perm} and r_{brine}) can be calculated as [37]:

$$r_{SOL}(y) = f_{s,SOL}\frac{\delta_{SOL}}{\sigma_{SOL}(y)} \qquad (A\ 13)$$

where δ_{SOL} (m) is the channel thickness, $f_{s,SOL}(-)$ is the shadow factor that takes into account the increase of the resistance due to the non-conductive spacer, σ_{SOL} (S m^{-1}) is the solution conductivity.

Finally, the model provides the distributed pressure drop, ΔP_{SOL}, [44] according to:

$$\frac{\Delta P_{SOL}(y)}{y} = \frac{1}{2}f \frac{\rho_{SOL}(y)\ u_{SOL}^2}{\delta_{SOL}} \qquad (A\ 14)$$

32

where ρ_{SOL} is the solution density, f is the Darcy friction coefficient, deriving from f *vs Reynolds number* CFD correlations [44], and u_{SOL} is the average solution superficial velocity, defined as:

$$u_{SOL} = \frac{Q_{SOL}}{b\,\delta_{SOL}} \qquad\qquad (A\ 15)$$

Appendix B. Experimental setup

Figure B1 shows the schematic representation of the experimental setup of tests presented in [43]. Inlet solutions were pumped to the stack at a flow rate of $\approx$18 l h^{-1} to maintain a fixed velocity of around $\approx$2 cm s^{-1} and pressure drops were monitored by the use of online manometers. For each solution, a valve was positioned after the stack, followed by a flowmeter to set the same channel pressure and monitor the flow rate. Increasing voltage steps were applied via a DC power supply (1902B, B&K precision) connected to the electrodes. The corresponding current was measured with a multimeter connected in series with the stack. Outlet brine and permeate conductivities were also measured with a portable conductivity meter.
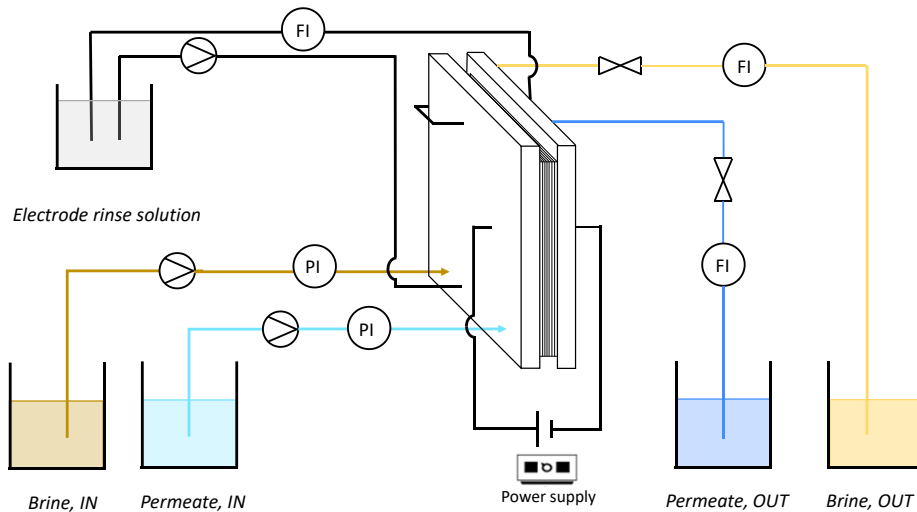
Figure B1. Schematic representation of the experimental setup (adapted from [43]**).**

The model was calibrated using tests with synthetic single-salt solutions (NaHCO$_3$) and validated with mixed salts solution with compositions reported in Table B1, mimicking the brine composition obtained by treating Seine River water with three RO stages. A Na$_2$SO$_4$ solution was used as electrode rinse solution. During each test, for both brine and permeate, inlet conductivity was measured before starting the test while the outlet conductivity was measured for each applied voltage after reaching steady state conditions. For mixed-salts synthetic solutions, chromatograph analysis was carried out to estimate the ionic composition.

Table B1. Ionic composition and conductivity for brine synthetic solutions.

	Ca^{2+} (mg l^{-1})	$Mg^{2+\ -1}$ (mg l^{-1})	Na^+ (mg l^{-1})	K^+ (mg l^{-1})	Cl^- (mg l^{-1})	SO_4^{2-} (mg l^{-1})	HCO_3^- (mg l^{-1})	Cond (mS cm^{-1})
Single salt NaHCO₃	-	-	860	-	-	-	2282	3.0
Mixed salts solution	343	78	92	1	300	66	1095	2.2

Appendix C. Simulated conditions

A more detailed table of the simulation plan is reported in Table C1.

Table C1. Operating condition for the simulation campaign for the 4 schemes reported in Figure 3. Simulations were performed at velocity of 10 cm s^{-1} along the stack (flow rate of 3.6 m^3 h^{-1}) for both permeate and brine, respectively.

Scheme	$Q_{perm,RO}$ (m^3 h^{-1})	$Q_{brine,RO}$ (m^3 h^{-1})	$Q_{perm,F\&B}$ (m^3 h^{-1})	$Q_{brine,F\&B}$ (m^3 h^{-1})	$Q_{perm,bypass}$ (m^3 h^{-1})	$\sigma_{perm,IN}$ (μS cm^{-1})	$\sigma_{perm,after\ mix}$ (μS cm^{-1})
Scheme 3a	3.6	0.6	-	3	-	10	260
	3.6	0.6	-	3	-	10	186
Scheme 3b	3	0.5	0.6	3.1	-	52	260
	2.7	0.5	0.9	3.1	-	73	260
	2.8	0.5	0.9	3.1	-	52	186
	2.3	0.4	1.3	3.2	-	73	186
Scheme 3c	3.4*	0.6	0.2	3	-	24	260
			0.7		0.5	70	
			1		0.8	100	
			1.2		1	130	
			1.4		1.2	160	
	4.5	0.8	-	2.8	0.9	10	260
			0.6		1.5	70	
			0.8		1.7	100	
			1		1.9	130	
			1.1		2.1	160	
	5.7	1	-	2.6	2.1	10	260
			0.5		2.6	70	
			0.7		2.7	100	
			0.8		2.9	130	
			1		3.1	160	
	8.5	1.5	-	2.1	4.9	10	260
			0.3		5.2	70	
			0.5		5.4	100	
			0.6		5.5	130	
			0.7		5.6	160	
	14.2	2.5	-	1.1	10.6	10	260
			0.2		10.8	70	
			0.3		10.9	100	
			0.4		11	130	
			0.5		11	160	
	19.8	3.5	-	0.1	16.2	10	260

			0.2		16.4	70	
			0.2		16.5	100	
			0.3		16.5	130	
			0.4		16.6	160	
Scheme 3d	25.5	4.5*	-	-	21.9	10	260
			0.1		22	70	
			0.2		22.1	100	
			0.2		22.1	130	
			0.2		22.2	160	
	31.2	5.5*	-	-	27.6	10	260
			0.1		27.7	70	
			0.2		27.7	100	
			0.2		27.8	130	
			0.2		27.8	160	
	36.8	6.5*	-	-	33.2	10	260
			0.1		33.3	70	
			0.1		33.4	100	
			0.2		33.4	130	
			0.2		33.4	160	
	42.5	7.5*	-	-	38.9	10	260
			0.1		39.0	70	
			0.1		39.0	100	
			0.1		39.0	130	
			0.1		39.1	160	

*For these conditions only a fraction of the total $Q_{brine,RO}$, equal to 3.6 m^3 h^{-1}, was fed to the pilot in order to guarantee the flow velocity of 10 cm s^{-1} in the stack.

REFERENCES

[1] K.H. Chu, J. Lim, S.J. Kim, T.U. Jeong, M.H. Hwang, Determination of optimal design factors and operating conditions in a large-scale seawater reverse osmosis desalination plant, J. Clean. Prod. 244 (2020) 118918. https://doi.org/10.1016/j.jclepro.2019.118918.

[2] L.N. Nthunya, M.F. Bopape, O.T. Mahlangu, B.B. Mamba, B. Van der Bruggen, C.A. Quist-Jensen, H. Richards, Fouling, performance and cost analysis of membrane-based water desalination technologies: A critical review, J. Environ. Manage. 301 (2022) 113922. https://doi.org/10.1016/j.jenvman.2021.113922.

[3] J. Raich-Montiu, J. Barios, V. Garcia, M.E. Medina, F. Valero, R. Devesa, J.L. Cortina, Integrating membrane technologies and blending options in water production and distribution systems to improve organoleptic properties. The case of the Barcelona Metropolitan Area, J. Clean. Prod. 69 (2014) 250–259. https://doi.org/10.1016/j.jclepro.2014.01.032.

[4] R. López-Roldán, S. Platikanov, J. Martín-Alonso, R. Tauler, S. González, J.L. Cortina, Integration of Ultraviolet-Visible spectral and physicochemical data in chemometrics analysis for improved discrimination of water sources and blends for application to the complex drinking water distribution network of Barcelona, J. Clean. Prod. 112 (2016) 4789–4798. https://doi.org/10.1016/j.jclepro.2015.06.074.

[5] A. Panagopoulos, K.J. Haralambous, M. Loizidou, Desalination brine disposal methods and treatment technologies - A review, Sci. Total Environ. 693 (2019) 133545. https://doi.org/10.1016/j.scitotenv.2019.07.351.

[6] A.S. Bello, N. Zouari, D.A. Da'ana, J.N. Hahladakis, M.A. Al-Ghouti, An overview of brine management: Emerging desalination technologies, life cycle assessment, and metal recovery methodologies, J. Environ. Manage. 288 (2021) 112358. https://doi.org/10.1016/j.jenvman.2021.112358.

[7] M. Khan, M.A. Al-Ghouti, DPSIR framework and sustainable approaches of brine management from seawater desalination plants in Qatar, J. Clean. Prod. 319 (2021) 128485.

https://doi.org/10.1016/j.jclepro.2021.128485.

[8]   EU Drinking Water Directive, (Council Directive 98/83/EC of 3 November 1998 on the quality of water intended for human consumption), n.d. https://ec.europa.eu/environment/water/water-drink/legislation_en.html%0A%0A.

[9]   J. Liang, A. Deng, R. Xie, M. Gomez, J. Hu, J. Zhang, C.N. Ong, A. Adin, Impact of seawater reverse osmosis (SWRO) product remineralization on the corrosion rate of water distribution pipeline materials, Desalination. 311 (2013) 54–61. https://doi.org/10.1016/j.desal.2012.11.010.

[10]   P. Nativ, O. Leifman, O. Lahav, R. Epsztein, Desalinated brackish water with improved mineral composition using monovalent-selective nanofiltration followed by reverse osmosis, Desalination. 520 (2021) 115364. https://doi.org/10.1016/j.desal.2021.115364.

[11]   J. Wu, M. Cao, D. Tong, Z. Finkelstein, E.M.V. Hoek, A critical review of point-of-use drinking water treatment in the United States, Npj Clean Water. 4 (2021) 1–25. https://doi.org/10.1038/s41545-021-00128-z.

[12]   O. Lahav, L. Birnhack, Quality criteria for desalinated water following post-treatment, Desalination. 207 (2007) 286–303. https://doi.org/10.1016/j.desal.2006.05.022.

[13]   A. Withers, Options for recarbonation, remineralisation and disinfection for desalination plants, Desalination. 179 (2005) 11–24. https://doi.org/10.1016/j.desal.2004.11.051.

[14]   H. Shemer, R. Semiat, D. Hasson, Re-mineralization of desalinated water using a mixture of CO_2 and H_2SO_4, Desalination. 467 (2019) 170–174. https://doi.org/10.1016/j.desal.2019.06.017.

[15]   H. Shemer, D. Hasson, R. Semiat, M. Priel, N. Nadav, A. Shulman, E. Gelman, Remineralization of desalinated water by limestone dissolution with carbon dioxide, Desalin. Water Treat. 51 (2013) 877–881. https://doi.org/10.1080/19443994.2012.694236.

[16]   L. Birnhack, S. Oren, O. Lehmann, O. Lahav, Development of an additional step to current CO_2-based $CaCO_3(s)$ dissolution post-treatment processes for cost-effective Mg^{2+} supply to desalinated water, Chem. Eng. J. 160 (2010) 48–56. https://doi.org/10.1016/j.cej.2010.03.002.

[17]   L. Birnhack, O. Lahav, Post-Treatment of Desalinated Water-Chemistry, Design, Engineering, and Implementation, Elsevier Inc., 2018. https://doi.org/10.1016/B978-0-12-809240-8.00008-3.

[18]   M.G. Biyoune, A. Atbir, H. Bari, L. Hassnaoui, E. Mongach, A. Khadir, L. Boukbir, R. Bellajrou, M. Elhadek, Remineralization of permeate water by calcite bed in the Daoura's plant (south of Morocco), Eur. Phys. J. Spec. Top. 226 (2017) 931–941. https://doi.org/10.1140/epjst/e2016-60181-6.

[19]   M.G. Biyoune, B. Bouargane, H. Bari, A. Marrouche, R. Bellajrou, A. Atbir, L. Boukbir, S. Mançour Billah, Water quality depends on remineralization's method in the desalination plant, Mediterr. J. Chem. 10 (2020) 162–170. https://doi.org/10.13171/mjc10202002141228mgb.

[20]   H. Shemer, D. Hasson, R. Semiat, State-of-the-art review on post-treatment technologies, Desalination. 356 (2015) 285–293. https://doi.org/10.1016/j.desal.2014.09.035.

[21]   S. Indika, Y. Wei, D. Hu, J. Ketharani, T. Ritigala, T. Cooray, M.A.C.K. Hansima, M. Makehelwala, K.B.S.N. Jinadasa, S.K. Weragoda, R. Weerasooriya, Evaluation of performance of existing ro drinking water stations in the north central province, sri lanka, Membranes (Basel). 11 (2021). https://doi.org/10.3390/membranes11060383.

[22]   N. Voutchkov, Re-mineralization of Desalinated Water Re-mineralization of Desalinated Water A SunCam online continuing education course, (n.d.). www.SunCam.com.

[23]   F. El Azhar, M. Tahaikt, N. Zouhri, A. Zdeg, M. Hafsi, K. Tahri, H. Bari, M. Taky, M. Elamrani, A. Elmidaoui, Remineralization of Reverse Osmosis (RO)-desalted water for a Moroccan desalination plant: Optimization and cost evaluation of the lime saturator post, Desalination. 300 (2012) 46–50. https://doi.org/10.1016/j.desal.2012.06.003.

[24]   O. Lehmann, L. Birnhack, O. Lahav, Design aspects of calcite-dissolution reactors applied for post treatment of desalinated water, Desalination. 314 (2013) 1–9.

https://doi.org/10.1016/j.desal.2012.12.017.

[25] Y.C. Kim, H. Yoon, Exploitation of acetic acid for calcite dissolution in small-capacity desalination plants, Desalination. 516 (2021) 115227. https://doi.org/10.1016/j.desal.2021.115227.

[26] A. Lesimple, F.E. Ahmed, N. Hilal, Remineralization of desalinated water: Methods and environmental impact, Desalination. 496 (2020) 114692. https://doi.org/10.1016/j.desal.2020.114692.

[27] T. Rijnaarts, W.M. De Vos, W.G.J. van der Meer, Method for the production of drinking water, WO2020067893A1, 2020.

[28] S.C.N. Tang, L. Birnhack, P. Nativ, O. Lahav, Highly-selective separation of divalent ions from seawater and seawater RO retentate, Sep. Purif. Technol. 175 (2017) 460–468. https://doi.org/10.1016/j.seppur.2016.10.030.

[29] S.C.N. Tang, L. Birnhack, Y. Cohen, O. Lahav, Selective separation of divalent ions from seawater using an integrated ion-exchange/nanofiltration approach, Chem. Eng. Process. Process Intensif. 126 (2018) 8–15. https://doi.org/10.1016/j.cep.2018.02.015.

[30] P. Nativ, N. Fridman-Bishop, O. Nir, O. Lahav, Dia-nanofiltration-electrodialysis hybrid process for selective removal of monovalent ions from Mg2+ rich brines, Desalination. 481 (2020) 114357. https://doi.org/10.1016/j.desal.2020.114357.

[31] Y. Tanaka, Ion-exchange membrane electrodialysis program and its application to multi-stage continuous saline water desalination, Desalination. 301 (2012) 10–25. https://doi.org/10.1016/j.desal.2012.06.007.

[32] L. Gurreri, A. Filingeri, M. Ciofalo, A. Cipollina, M. Tedesco, A. Tamburini, G. Micale, Electrodialysis with asymmetrically profiled membranes: Influence of profiles geometry on desalination performance and limiting current phenomena, Desalination. 506 (2021) 115001. https://doi.org/10.1016/j.desal.2021.115001.

[33] G.J. Doornbusch, M. Bel, M. Tedesco, J.W. Post, Z. Borneman, K. Nijmeijer, Effect of membrane area and membrane properties in multistage electrodialysis on seawater desalination performance, J. Memb. Sci. 611 (2020) 118303. https://doi.org/10.1016/j.memsci.2020.118303.

[34] R.A. Tufa, S. Pawlowski, J. Veerman, K. Bouzek, E. Fontananova, G. di Profio, S. Velizarov, J. Goulão Crespo, K. Nijmeijer, E. Curcio, Progress and prospects in reverse electrodialysis for salinity gradient energy conversion and storage, Appl. Energy. 225 (2018) 290–331. https://doi.org/10.1016/j.apenergy.2018.04.111.

[35] W.Z. Cui, Z.Y. Ji, K. Tumba, Z. De Zhang, J. Wang, Z.X. Zhang, J. Liu, Y.Y. Zhao, J.S. Yuan, Response of salinity gradient power generation to inflow mode and temperature difference by reverse electrodialysis, J. Environ. Manage. 303 (2022) 114124. https://doi.org/10.1016/j.jenvman.2021.114124.

[36] M. Vanoppen, E. Criel, G. Walpot, D.A. Vermaas, A. Verliefde, Assisted reverse electrodialysis—principles, mechanisms, and potential, Npj Clean Water. 1 (2018). https://doi.org/10.1038/s41545-018-0010-1.

[37] M. La Cerva, L. Gurreri, A. Cipollina, A. Tamburini, M. Ciofalo, G. Micale, Modelling and cost analysis of hybrid systems for seawater desalination: Electromembrane pre-treatments for Reverse Osmosis, Desalination. 467 (2019) 175–195. https://doi.org/10.1016/j.desal.2019.06.010.

[38] M. Vanoppen, E. Criel, S. Andersen, A.R.D. Verliefde, Assisted Reverse Electrodialysis : a Novel Technique To decrease reverse osmosis energy demand, AWWA / AMTA Membr. Technol. Conf. Pap. 32 (2016) 1–12. https://biblio.ugent.be/publication/7098263.

[39] Z.Y. Guo, Z.Y. Ji, Q.B. Chen, J. Liu, Y.Y. Zhao, F. Li, Z.Y. Liu, J.S. Yuan, Prefractionation of LiCl from concentrated seawater/salt lake brines by electrodialysis with monovalent selective ion exchange membranes, J. Clean. Prod. 193 (2018) 338–350. https://doi.org/10.1016/j.jclepro.2018.05.077.

[40] W. Li, W.B. Krantz, E.R. Cornelissen, J.W. Post, A.R.D. Verliefde, C.Y. Tang, A novel hybrid process of reverse electrodialysis and reverse osmosis for low energy seawater desalination and brine management, Appl. Energy. 104 (2013) 592–602. https://doi.org/10.1016/j.apenergy.2012.11.064.

[41] V. V. Wagholikar, H. Zhuang, N.E. Moe, J. Barber, H. Ramanan, J.Y.H. Fuh, Analysis of RED/dRED stack performance using a resistances in series model, Desalination. 496 (2020) 114505. https://doi.org/10.1016/j.desal.2020.114505.

[42] M. Turek, B. Bandura, P. Dydo, Electrodialytic boron removal from SWRO permeate, Desalination. 223 (2008) 17–22. https://doi.org/10.1016/j.desal.2007.01.181.

[43] M. Philibert, A. Filingeri, C. Natalello, N. Moe, E. Filloux, A. Cipollina, Surface water RO permeate remineralization through minerals recovery from brines, Desalination. 531 (2022) 115725. https://doi.org/10.1016/j.desal.2022.115725.

[44] M.L. La Cerva, M. Di Liberto, L. Gurreri, A. Tamburini, A. Cipollina, G. Micale, M. Ciofalo, Coupling CFD with a one-dimensional model to predict the performance of reverse electrodialysis stacks, J. Memb. Sci. 541 (2017) 595–610. https://doi.org/10.1016/j.memsci.2017.07.030.

[45] L. Gurreri, A. Tamburini, A. Cipollina, G. Micale, M. Ciofalo, CFD prediction of concentration polarization phenomena in spacer-filled channels for reverse electrodialysis, J. Memb. Sci. 468 (2014) 133–148. https://doi.org/10.1016/j.memsci.2014.05.058.

[46] L. Gurreri, M. Ciofalo, A. Cipollina, A. Tamburini, W. Van Baak, G. Micale, CFD modelling of profiled-membrane channels for reverse electrodialysis, Desalin. Water Treat. 55 (2015) 3404–3423. https://doi.org/10.1080/19443994.2014.940651.

[47] A.H. Galama, N.A. Hoog, D.R. Yntema, Method for determining ion exchange membrane resistance for electrodialysis systems, Desalination. 380 (2016) 1–11. https://doi.org/10.1016/j.desal.2015.11.018.

[48] S.J. Duranceau, R.J. Wilder, S.S. Douglas, Guidance and recommendations for posttreatment of desalinated water, J. Am. Water Works Assoc. 104 (2012). https://doi.org/10.5942/jawwa.2012.104.0119.

[49] M. Philibert, E. Filloux, C. Garriou, D. Steinmann, A. Cipollina, Installation and process for providing mineralized drinking water, European Patent EP19306565, 2019.

[50] J.W. Post, H. Huiting, E.R. Cornelissen, H.V.M. Hamelers, Pre-desalination with electro-membranes for SWRO, Desalin. Water Treat. 31 (2011) 296–304. https://doi.org/10.5004/dwt.2011.2400.

[51] H. Lu, W. Zou, P. Chai, J. Wang, L. Bazinet, Feasibility of antibiotic and sulfate ions separation from wastewater using electrodialysis with ultrafiltration membrane, J. Clean. Prod. 112 (2016) 3097–3105. https://doi.org/10.1016/j.jclepro.2015.09.091.

[52] D. Ankoliya, A. Mudgal, M.K. Sinha, P. Davies, E. Licon, R.R. Alegre, V. Patel, J. Patel, Design and optimization of electrodialysis process parameters for brackish water treatment, J. Clean. Prod. 319 (2021). https://doi.org/10.1016/j.jclepro.2021.128686.

[53] I. Renewable, E. Agency, Renewable Technology Innovation Indicators : Mapping progress in costs , patents and standards, n.d.

[54] K. Dai, J.L. Wen, Y.L. Wang, Z.G. Wu, P.J. Zhao, H.H. Zhang, J.J. Wang, R.J. Zeng, F. Zhang, Impacts of medium composition and applied current on recovery of volatile fatty acids during coupling of electrodialysis with an anaerobic digester, J. Clean. Prod. 207 (2019) 483–489. https://doi.org/10.1016/j.jclepro.2018.10.019.

[55] L. Birnhack, N. Voutchkov, O. Lahav, Fundamental chemistry and engineering aspects of post-treatment processes for desalinated water-A review, Desalination. 273 (2011) 6–22. https://doi.org/10.1016/j.desal.2010.11.011.

[56] M. La Cerva, L. Gurreri, M. Tedesco, A. Cipollina, M. Ciofalo, A. Tamburini, G. Micale, Determination of limiting current density and current efficiency in electrodialysis units, Desalination. 445 (2018) 138–148. https://doi.org/10.1016/j.desal.2018.07.028.

[57] A. Campione, A. Cipollina, I.D.L. Bogle, L. Gurreri, A. Tamburini, M. Tedesco, G. Micale, A hierarchical model for novel schemes of electrodialysis desalination, Desalination. 465 (2019) 79–93. https://doi.org/10.1016/j.desal.2019.04.020.

[58] M. Yizhak, Ions in Solution and their Solvation, 2015.

[59] K.S. Pitzer, G. Mayorga, Thermodynamics of electrolytes. II. Activity and osmotic coefficients for 2-2 electrolytes,, J. Solut. Chem. 3 (1974) 539–546, https://doi.org/ 10.1007/BF00648138., n.d.